Elucidating how correlated operation of shear transformation zones leads to shear localization and fracture in metallic glasses: tensile tests on Cu-Zr based metallic-glass microwires, molecular dynamics simulations, and modelling

K.F. Gan[1], S.S. Jiang[2], Y.J. Huang[2], H.B.C. Yin[2], J.F. Sun[2], A.H.W. Ngan[1]*

[1]*Department of Mechanical Engineering, The University of Hong Kong, Pokfulam Road,*

Hong Kong, People's Republic of China

[2]*School of Materials Science and Engineering, Harbin Institute of Technology, Harbin 150001, People's Republic of China*

* Corresponding author (email: hwngan@hku.hk)

Abstract

The plastic deformation of metallic glasses (MG) is well-known to occur via shear transformation zones (STZs) on the scale of atomic clusters, yet fracture of MG takes place via shear bands of the micron scale. So far, understanding on how the operation of STZs leads to shear localization and fracture remains limited. In this work, tensile tests on Cu/Zr-based MG micro-wires show that both the first-yield and fracture stress exhibit the Weibull distribution, and fractography reveals that shear localization in the form of intense shear bands leads to shear fracture. Molecular dynamics (MD) simulations show that shear bands form via the correlated emergence and operation of discrete STZs close to one another. To describe how the stochastic yet correlated occurrence of the discrete STZs leads to shear localization, a model is constructed to relate the probability of the successive operation of discrete STZs, to their nucleation density. The model predicts that, if nucleation density of the STZs grows along the strain path, as prior shear events triggers the emergence of new STZs, then successive occurrence of discrete shear events speeds up rapidly to an asymptotic state which is exactly the condition of shear localization and shear banding. Furthermore, the MD results suggest an exponential growth law for the occurrence of the STZs along the strain path, which also gives predictions in good agreement with the experimental Weibull distributions of the first-yield stress of Cu/Zr-based MGs.

Keywords: metallic glass; shear localization; stochastic deformation; shear transformation zones; shear bands

1. Introduction

Bulk metallic glasses (BMGs) have attracted considerable attention due to their ultra-high strength and elastic limit (Guo et al., 2007b; Ramamurty et al., 2005; Xu et al., 2005). While the deformation of BMGs near or above glass transition temperature exhibits a homogenous behavior with significant inelasticity, their plastic deformation at low temperatures is limited and exhibits strong scattering (Liu et al., 2007; Lu et al., 2003; Ramamurty et al., 2005; Schuh et al., 2007; Sopu et al., 2017; Zhao et al., 2013). The plastic deformation of BMGs is widely believed to be associated with shear banding, for which a number of theories have been proposed (Fornell et al., 2009; Greer et al., 2013; Jang et al., 2011; Sopu et al., 2017; Yoo et al., 2012). First, the homogenous nucleation theory stipulates the thermal activation of shear bands via shear transformation zones (STZs) or geometrically unfavored motifs (GUMs) homogeneously distributed in the prefect BMG matrix (Ding et al., 2014; Greer et al., 2013; Maaß and Löffler, 2015; Sopu et al., 2017; Xu et al., 2018; Zhao et al., 2013). Secondly, the aged-rejuvenation-glue-liquid (ARGL) model of heterogeneous nucleation considers that the inevitable cast imperfections can facilitate shear band nucleation as they act as stress concentrators (Shimizu et al., 2006; Xu et al., 2018; Zhao et al., 2013), which create an embryonic shear front comprising four parts, namely, an aged glass zone, a rejuvenation-tip zone, a glue zone and a liquid zone. In this mechanism, the neonatal front of the shear band propagates into the adjacent well-aged glass matrix during deformation. The third mechanism considers the formation of a shear band as involving a first stage in which a viable band is created and shears by structural rejuvenation, and a second stage in which synchronized sliding occurs to shear off along the rejuvenation plane (Greer et al., 2013; Klaumünzer et al., 2011).

Although a lot of understanding has already been gained on the nucleation and propagation of shear bands in BMGs, the conditions at which catastrophic fracture happens are much less understood. In general, catastrophic fracture is found to occur soon after incipient yielding at room temperature (Bletry et al., 2006; Liu et al., 2010; Maaß and Löffler, 2015), and it was postulated that dense shear bands observed at surfaces of deformed BMG samples are a result of localized strain softening from free volume accumulation (Argon, 1979; Zhu et al., 2017). A number of studies have been carried out to understand localized deformation and fracture in general (Carroll et al., 2012; Chung et al., 2014; Huespe et al., 2012; Sun et al., 2009). For instance, a finite deformation generalization of the finite thickness embedded discontinuity formulation was proposed for the analysis of ductile fracture, which provided a constitutive picture of local straining prior to fracture (Huespe et al., 2012). For dual-phase structured steels, ductile fracture was modeled in the form of plastic strain localization due to the incompatible deformation between the dual phases (Sun et al., 2009). Localization of strain fields in metallic glasses was also investigated via *in-situ* digital image correction, which indicated that ductility was due to the intrinsic structural heterogeneities and the evolution of localized strain plays an important role on the formation of shear bands (Wu et al., 2015). However, the physical conditions that lead to such strain localization along with catastrophic fracture in brittle metallic glasses still remain unclear. The purpose of this work is therefore to gain deeper insight into the strain localization conditions in BMGs that undergoes plastic deformation and shear fracture by discrete shear band nucleation and propagation. In the following, the stochastic nature of deformation and fracture is first appreciated from tensile experiments on Cu/Zr-based BMG microwires and molecular dynamics (MD) simulations on nano-sized simulation samples. Then, we propose a stochastic model to describe the condition of strain localization, and apply it to reconcile the experimental results. Appendix 1 gives a glossary of terms used throughout the paper.

2. Experimental Features of Deformation of BMG Microwires

The fracture of a material is conveniently revealed by tensile testing and furthermore, melt extraction is a process that can produce MG microwires in large quantities ready for tensile testing. For this reason, tensile tests were carried out on micro-wires of three types of melt-extracted Cu/Zr-based metallic glasses (MGs), namely, $Cu_{46.5}Zr_{46.5}Al_7$, $Cu_{48}Zr_{48}Al_4$ and $Cu_{47.5}Zr_{48}Al_4Nb_{0.5}$ (Jiang et al., 2018; Shen et al., 2014a; Shen et al., 2014b). The melt-extraction technique has been greatly optimized over time and is capable of producing MG microwires with smooth surface and few casting flaws. The diameters of the micro-wires used in the subsequent tensile testing were measured by SEM to be respectively 46.29 ± 1.06 μm for $Cu_{46.5}Zr_{46.5}Al_7$, 45.57 ± 0.54 μmfor $Cu_{48}Zr_{48}Al_4$, and 45.86 ± 1.15 μm for $Cu_{47.5}Zr_{48}Al_4Nb_{0.5}$. The microwires were cut into different lengths and were glued by epoxy resin onto paper templates with diamond-shape windows of different sizes. After mounting each specimen-template assembly onto the air-pressure grips of the micro-tensile tester (INSTRON 5848), the two sides of the paper template were cut open to free out the glued metallic glass microwire (Chen and Ngan, 2012). As such, the gage lengths of the samples were 12mm, 30mm or 60mm. Before the tests, the samples were checked again with optical microscopy, and any ones with large visible surface flaws or bending segments were certified then discarded. The tensile tests were carried out at room temperature of ~20 °C, at a constant load rate of ~500MPa/s until the microwire fractured. Tests in which the wires fractured outside the gage length, i.e. inside or near the glued parts in the grips, were neglected. In order to investigate the scattering nature of the deformation, the test was repeated over 20 times for specimens of the same BMG and gage length. After tensile testing, all fractured segments were collected and cleaned with ethyl alcohol, for subsequent examination in a Hitachi S-4800FEG SEM. As mentioned above, samples with visible artificial surface flaws, non-sufficient uniform diameter, or misalignment on the template, were discarded, since such subtle imperfections in the test geometry may dramatically influence the deformation response of metallic glass specimens (Wu et al., 2008).

2.1 Stress-strain behavior and microstructures

Fig. 1(a-c) show typical stress-strain curves of the three types of BMG microwires tested. The end of each curve denotes the fracture point, and the first yield point is marked by an arrow. In the initial stage of deformation, all strain-stress curves generally exhibit a smooth and continuous elastic behavior, and then, a sudden deviation from the initial linear behavior occurs, and this is identified as the first-yield point σ_y. After that, fracture soon occurred at stress σ_f.

SEM examination of the surface morphology of the MG microwires revealed discrete shear bands as the main signs of plastic deformation, as shown in the case of $Cu_{48}Zr_{48}Al_4$ in Fig. 2. Of particular interest is the observation that the distribution of shear bands is highly inhomogeneous, and in locations close to the fracture, the number of shear bands is intense. The evidence here indicates that shear events are highly localized.

2.2 Weibull distributions for first-yield and fracture stress

As shown in Fig. 1(a), in the case of the $Cu_{46.5}Zr_{46.5}Al_7$ alloy, the strengths of the samples scatter significantly, but a clear trend of “longer being weaker” size effect is not observed. Fig. 3(a, c, e) show the Weibull plot of the strength data of the three types of alloys, according to (Weibull, 1951):

$$F(\sigma) = \exp[-V(\sigma/\sigma_0)^m]. \tag{1}$$

where σ is σ_y or σ_f, m is the Weibull modulus, and σ_0 is a scaling parameter. The volume of the tested samples V is the gauge length (12 mm, 30 mm or 60 mm) times the cross-sectional area of the wires which is common for all tested samples, and hence, V is proportional to the gauge length. The survival probability $F(\sigma)$ is calculated by $F(\sigma_i) = 1 - i/(N+1)$, where N is the total number of tested specimens in each group, and i is the rank in ascend order of the yield or fracture stresses σ_i in the group (Pugno and Ruoff, 2006; Qin et al., 2013; Zhao et al., 2008). The double logarithmic plots in Fig. 3(a, c, e) show that although eqn. (1) is roughly obeyed for a given gauge length or sample volume V, for each alloy the plots for different gauge lengths or V do not collapse into a single trend. Therefore, the tensile test data from all of the three alloys do not obey eqn. (1), with V being the entire volume of the sample.

In Fig. 3(b, d, f), $\ln\ln(1/F)$, instead of $\ln\ln(1/F) - \ln V$, is plotted against $\ln\sigma_y$ or $\ln\sigma_f$. It can be seen that, for each alloy, the discrepancies between different groups of gauge length have remarkably reduced, compared to the case when $\ln\ln(1/F) - \ln V$ is plotted against $\ln\sigma_y$ or $\ln\sigma_f$ in Fig. 3(a, c, e). In particular, data from different gauge lengths now approximately collapse into a single trend, describable by

$$F(\sigma) = \exp[-\Omega(\sigma/\sigma_0)^m] \tag{2}$$

where Ω is a volume parameter independent of the gauge length of the sample. In Fig. 4, instead of separately plotting the data from different gauge lengths, all data from different gauge lengths are pooled together and ranked without referencing to their gauge lengths, and new survivability probability is assigned according to $F(\sigma_i) = 1 - i/(N+1)$ where i is the rank in the combined pool, and N its size. It can be seen that, for a given alloy, eqn. (2) is obeyed with Ω being an arbitrary constant independent of the volume of the sample.

The fact that eqn. (2) (with a constant Ω) rather than eqn. (1) (with V being the volume of the entire sample) is obeyed for a volume Ω independent of the gage length is intriguing. To shed light on this and other aspects of the deformation, molecular dynamics (MD) simulations were carried out, as detailed below.

3. Insights from Molecule Dynamics (MD) Simulations

Molecule dynamics (MD) simulations were performed using the LAMMPS code (Plimpton, 1995; Sha et al., 2014; Sopu et al., 2016). Atoms of Cu, Zr and Al were randomly distributed into a simulation cell to construct a glassy $Cu_{48}Zr_{48}Al_4$ sample, and embedded-atom-method (EAM) potentials (Cheng et al., 2009; Kaban et al., 2015) were used for the atomistic interactions. The constructed sample was a cuboid block with 22,221 atoms of the $Cu_{48}Zr_{48}Al_4$ composition with periodic boundary conditions (PBC) applied along all of three dimensions. The block was first equilibrated at 2300K for 2ns, then quenched from the melt state to 50K at a constant cooling rate of 10^{10}K/s at NPT condition, and then relaxed at 50K for 2ns. (Integration step time was 1fs.) Plate-shape metallic glass samples were produced via replicating the initial small glassy block into a large size ~6.7nm×20.5nm×133.1nm with ~1,066,600 atoms, followed by annealing at 800K for 0.5ns and taken back to 50K finally (Sha et al., 2014). Uniaxial tensile deformation was carried out on the replicated glassy plate along the z direction at a constant strain rate of 6×10^7/s, while three-dimensional PBCs were applied to avoid the occurrence of necking (Albe et al., 2013; Zhou et al., 2013). The atomistic deformation was investigated by visualizing the local atomic shear strain, calculated via the OVITO analyzing and visualization program (Shimizu et al., 2007; Şopu et al., 2011; Şopu et al., 2015).

Fig. 5(a) shows a typical set of simulation result for the deformation process of the metallic glass samples. Here, the simulated stress-strain curve shows the first sign of deviation from linearity at an overall tensile strain of $\varepsilon \sim 0.027$. To reveal the discrete shear transformation zones (STZs), the accumulative local shear strain around each atomic site is calculated with reference to the relaxed state before deformation (Luan et al., 2017; Sha et al., 2014; Sopu et al., 2017). The simulated snapshot in Fig. 5(a) at the noticeable yield point at which $\varepsilon \sim 0.027$ shows the atomic positions only with accumulative shear strains ≥ 0.2, whereas atoms with accumulative strains < 0.2 are not shown. Treating those atomic sites with accumulative shear strains ≥ 0.2 as the STZs, the snapshot in Fig. 5(a) indicates that at the noticeable yield point, STZs have already occurred sporadically in scattered places in the sample. Fig. 5(b) shows the development of the STZs after the yield point, and again, in each snapshot, discrete STZs (marked as green) are identified as locations with accumulative shear strains ≥ 0.2, whereas atoms with accumulative strains < 0.2 are not shown. It can be seen that, with increasing straining past the yield point (snapshot 1) discrete STZs tend to occur close to one another, and their coalesced operation leads to microscopic shear bands that run across the sample at ~45° to the long axis in the end. The first occurrence of clear shear bands takes place at total strain $\varepsilon \sim 0.078$ (snapshot 4), and this corresponds to the peak of the stress-strain curve in Fig. 5(a), after which the stress falls at the constant imposed strain rate due to the formation of more shear bands. To show the spatio-temporal correlation of the occurrence of the discrete STZs statistically, for each STZ i, its position and time of occurrence, namely $\vec{r_i}$ and t_i, were recorded during the tensile deformation at an interval of ~0.03% in the total strain. For every pair i and j of STZs, their distance Δr_{ij} and time interval of occurrence Δt_{ij} were calculated as:

$$\Delta r_{ij} = \left|\vec{r_i} - \vec{r_j}\right|, \tag{3}$$

$$\Delta t_{ij} = \left|t_i - t_j\right|, \tag{4}$$

and then the joint probability density $p(\Delta r, \Delta t)$ was obtained as

$$p(\Delta r, \Delta t) = \frac{1}{2N}\sum_{i,j}\frac{\delta(\Delta r - \Delta r_{ij})\delta(\Delta t - \Delta t_{ij})}{4\pi\Delta r^2} \tag{5}$$

where N is the total number of STZs. Fig. 5(c) shows the $p(\Delta r, \Delta t)$ at the initial stage of deformation before noticeable yielding, namely from strain 0 to ε ~ 0.027 in the MD simulation. At the simulated strain rate, it takes ~550ps to reach the noticeable yielding at ε = 0.027, while the STZs are mainly produced within the last ~40 ps of such a straining process close to the observable yield. This is why Fig. 5(c) shows high values of the probability density $p(\Delta r, \Delta t)$ at Δt ~ 40 ps; however, the STZs that emerge during this window of time are not spatially correlated, since the probability density spreads over a wide range of Δr values up to over 1 nm. Fig. 5(d) shows the $p(\Delta r, \Delta t)$ for the regime from the noticeable yielding at ε = 0.027 to ε = 0.076 at which clear shear bands have formed. It can be seen that the $p(\Delta r, \Delta t)$ peaks near $(\Delta r = 0, \Delta t = 0)$, indicating a high tendency for discrete STZs to occur very close to each other in both the space and time domains, within the strain regime from yielding to shear banding. The results in Fig. 5(c,d) indicate that near the noticeable yield point, plasticity is due to the uncorrelated operation of STZs at different locations in the sample, and then later on in the post-yield strain path, the occurrence of STZs begins to exhibit a strong correlation or localization effect, namely, the past operation of a STZ leaves behind a history effect in the neighborhood to trigger the occurrence of another STZ nearby. Eventually, the operation of such highly correlated STZs leads to a microscopic shear band locally. Fig. 5(e) shows the correlated emergence of STZs within the red box region Ω in Fig. 5(b) during a shear banding process, from snapshots 3 to 5 in (b) with overall strain ~0.072, ~0.075 and ~0.078 respectively. At each overall strain, the atomic positions with local accumulative strains over 0.2 are shown in the middle panel to indicate the STZs operated, and the right panel shows the positions of atoms with ΔE larger than 0.25 eV, where ΔE is the potential energy increment relative to the mean energy of the corresponding atomic species in the load-free state. The blue boxes mark regions where ΔE is high due to some operated STZs nearby, and the blue arrows indicate that in the next strain increment, new STZs emerge from these high-energy regions. The results here show a correlated behavior of STZs in which new STZs preferentially emerge at the high energy (or stress) locations near previously operated STZs.

Length independence of strength – The MD results here enable one to understand why the strength data from the present experiments in Figs. 1, 3 and 4 do not depend on the length of the BMG wire in a statistical sense. The MD simulation snapshot in Fig. 5(a) shows that at the noticeable yield point at which $\varepsilon \sim 0.027$, a rather large quantity of STZs have already emerged sporadically and operated in different, isolated sites of the sample. In Fig. 5(b), snapshot 2 shows that as the overall strain ε increases further past the yield point, the STZ quantity increases further throughout the sample. This is an important observation that will explain the length independence of strength of the micro-wires. If yielding were to mark the emergence and operation of a *single* discrete event such as a STZ, then the yield strength would have to depend on the sample volume V according to eqn. (1). This is because, if the survivability of a small material volume Ω against the emergence of a single event is $F_{\Omega}(\sigma)$, then, the survivability F of the entire sample V against yielding would be $F = [F_\Omega(\sigma)]^{V/\Omega}$, which would give $\ln\ln(1/F) - \ln V = -\ln\Omega + \ln\ln[1/F_\Omega(\sigma)]$. If this were the case for the observable yield in the present experiments, then the plots in Figs. 3(a, c, e) would have collapsed into single trends independent of V, since the right side of the above equation, namely, $-\ln\Omega + \ln\ln[1/F_\Omega(\sigma)]$, would depend on σ and not on V. Observable yield in the present experiments is evidently not due to the stochastic emergence of a single event such as a STZ. In fact, the strain scale in the plots in Fig. 1 suggests that at noticeable yield, the proof strain is already likely ~0.001, and for even the shortest wires of length 12 mm, the plastic elongation would be ~ 12 μm. Such an amount of displacement has to be due to the operation of a lot of STZs in the wire.

When discussing the formation of a discrete STZ in a statistical way, the atomic degrees of freedom (atomic positions and velocities) that are pertinent must be those within a small atomic cluster that contains only the eventual STZ plus its immediate neighborhood, i.e. a nucleus volume. The microwires used in the present experiments were 12 mm to 60 mm long and their diameters were ~45 μm, and so they would contain a huge number of such potential nucleating sites for STZs. With such a large quantities of STZ nuclei, the overall plastic strain of the wire is simply the average strain of all activated STZs in the wire, and so if the overall plastic strain is to be noticeable at some proof strain value of, say, 0.001, the average strain of the activated STZs has to be equal to this value too. Since all the volume elements of the STZ nuclei within the wire are subjected to rather similar stress state, they form a statistical ensemble in thermo-mechanical equilibrium, and the condition of observable yield becomes one of requiring a specific average strain from the ensemble. When interpreted in this way, since the number of STZ nuclei in the ensemble (i.e. the wire) is huge, the stress that leads to a specific average strain from the ensemble should not depend on the size of the ensemble. Therefore, the yield strength of the wires should not depend on their length in a statistical way, as is observed experimentally in Figs. 1, 3 and 4.

In addition to the first yield, Figs. 1, 3 and 4 also show that the fracture strength of the micro-wires does not depend on their length or volume, and the explanation is also similar to the above for the first yield. Shear fracture is evidently (see Fig. 2) due to the operation of intense slip bands. In the MD simulations in Fig. 5, since the PBC is used, fracture is not simulated directly, but the snapshots 4 to 7 in Fig. 5(b) showing the formation of multiple shear bands mark a sharp drop in the stress-strain curve (Fig. 5(a)) and hence an instability condition. Therefore, in a real wire near its fracture point, many shear bands should have occurred simultaneously along the wire, and the action of one extreme shear band leads to fracture (c.f. Fig. 2(a)).

In Fig. 5(b), the detailed formation of a microscopic shear band is shown in the regime framed by the red boxes in snapshots 3 to 5 in Fig. 5(b). Here, as the overall strain ε increases from 0.072 to 0.078 (snapshots 3 and 4), the occurrence of STZs suddenly speeds up in the framed region, where a few already operated STZs trigger the formation of a lot more STZs nearby in a highly correlated manner (c.f. Fig. 5(d, e)). This process eventually forms a discrete shear band that runs across the specimen thickness at ~ 45° with respect to the specimen axis, as snapshots 5 to 8 show. It is interesting to note that the majority of the already operated STZs in snapshot 3, in particular those outside the red box, do not trigger the accelerated formation of nearby STZs in snapshot 4, indicating the statistical nature of the correlated formation/operation of STZs. When discussing the formation of a microscopic shear band in a statistical way, the atomic degrees of freedom (atomic positions and velocities) that are pertinent must be those within a small, localized representative volume element (RVE) that contains only the eventual shear band plus its immediate neighborhood, namely, a region similar to the red box Ω in Fig. 5(b). Since the eventual shear band runs at ~ 45° with respect to the wire axis, Ω is approximately a section of the wire with length equal to the wire diameter. Therefore, again, since the present micro-wires in the experiments were 12 mm to 60 mm long, and so with the size of Ω estimated above, these wires would contain thousands of RVE's stacked together along the wire-axis direction. Such a large amount of RVE's would form an ergodic enough statistical ensemble in thermo-mechanical equilibrium, since all the RVEs along the wire are subjected to the same tensile loading as they are connected in series (Fig. 6). Now, unlike yield which requires a specific average strain from the ensemble, the criterion for shear fracture requires the distribution in the ensemble to be in such a way that the extreme RVE's produce a large enough shear to result in instability. But again, for an ergodic ensemble in equilibrium, the distribution of properties amongst its replicas should not depend on the ensemble size. Therefore, the fracture strength of the wires should not depend on their length in a statistical way, as is observed experimentally in Figs. 1, 3 and 4.

The yield and fracture of BMG micro-wires in fact bear some interesting analogy with the "global sharing" concept, as opposed to the "local sharing" or "weakest link" concept, in the discussion of statistical strength (Ibnabdeljalil and Curtin, 1997; Phoenix and Raj, 1992). In the "local load sharing" model, breakage of the weakest link raises stress in neighboring ones to make them break in a cascade manner, so that strength obeys a characteristic volume dependence. However, in the "global sharing" model, the stress change due to a broken link is shared globally by all remaining links, so that strength is determined by the ensemble behavior of all links rather than by the weakest one, and hence does not depend on volume. The yield and fracture of the present BMG micro-wires are determined by the ensemble behavior of the RVEs in terms of STZ operation, and so is akin to the "global sharing" concept without a volume dependence.

4. A Model for Shear Banding in Metallic Glasses

The MD results in the above section indicate that initial yield is due to the sporadic emergence and operation of STZs, and later on in the strain path, the operation of STZs becomes correlated locally, leading to shear localization in the form of shear banding, which eventually should correspond to the experimentally observed shear fracture at the end. As indicated in Fig. 5(b) (e.g. snapshot 7), although many shear bands can form simultaneously, the formation of each shear band should be determined by the atomic degrees of freedom within an RVE of a micro-scale volume Ω that contains the shear band plus its immediate neighborhood. Nanometric volumes of metallic glasses are in fact known to deform in a homogenous manner without strain localization (Guo et al., 2007a; Jang and Greer, 2010; Zhou et al., 2013; Zhou et al., 2015), and hence the RVE for shear banding has to be large enough to contain all the atomic degrees of freedom that are pertinent for the shear band to form; hence Ω is a micro-sized volume instead of being smaller. As mentioned above, since the eventual shear band in a micro-wire sample runs at ~ 45° with respect to the wire axis, Ω should be approximately a section of the wire with length equal to the wire diameter. Thus, along a wire of tens of mm long, a large number of RVEs would be stacked in series and they are subjected to the same applied load (Fig. 6); such an ensemble of RVEs forms a statistical-mechanics ensemble in thermo-mechanical equilibrium (Ngan, 2009) (i.e. the RVEs are subjected to the same stress state and temperature). Within each RVE, at sufficient applied load, a shear band may form due to the correlated emergence and operation of discrete STZs, as illustrated in Fig. 5(b). However, since the different RVEs in the ensemble have in general different internal structures, the shear banding may not be synchronized in the ensemble, so that at a given point in time, the shear band formation may be more mature in some RVEs and less in others (c.f. Fig. 5(b), e.g. snapshots 5 and 6). But it is the average behavior (i.e. strain) of the RVEs in the ensemble that gives the overall proof strain of the wire, or the extreme strain in the ensemble that determines the shear fracture. Then, it follows that understanding the statistical variability of the RVEs at different points in the load path would be critical in understanding yielding and fracture of BMGs.

Based on the above consideration, we develop a model here to account for the variability in the shear localization within the ensemble RVEs in a statistical way. This model is based on an ensemble concept which we used earlier to study a transition in deformation from stochastic to deterministic behavior (Ngan and Ng, 2010), and here, we further develop it to predict shear localization in the form of shear banding. Consider a large ensemble of such RVEs, as shown in Fig. 6, with identical shapes and dimensions but varying individual microstructures, subjected to the same load simultaneously. Due to their varying microstructures, the sequential occurrence of discrete STZs (labelled by their order of emergence $k = 1, 2, 3$, etc.) amongst the RVE replicas are not necessarily synchronized. Let Ω be the volume of each RVE in the ensemble, and F_k be the ensemble survivability against the k^{th} discrete STZ, namely, F_k is the fraction of the RVEs in the ensemble in which the k^{th} STZ has not yet occurred. Meanwhile, by considering the average microstructure in the RVE replicas, we define n_k to be the density of potential sites (i.e. nuclei) from which the k^{th} STZ can emerge, i.e. n_k is the number of STZ nuclei per unit volume, averaged from all the RVEs in the ensemble. Supposing there are N RVEs in the ensemble, then, the number of RVEs that are potent to produce the k^{th} STZ at a given time point at site i is $(F_k - F_{k-1})N$. Among these potent RVEs, by definition of n_k above, the total number of STZ nuclei is $n_k\,\Omega\,(F_k - F_{k-1})N$ at a given time instant. Operation of these STZ nuclei will lead to a reduction $d(F_kN)$ of the number of RVEs in which the k^{th} event has not occurred; hence,

$$(F_k - F_{k-1})\frac{dn_k}{dL}\Omega = -\frac{dF_k}{dL} \tag{6}$$

where L is a convenient load-path variable, such as time, or load in a load-controlled test. Specifically, dn_k/dL is the occurrence rate of the density of nuclei for the k^{th} STZ with respect to the variable L; if dn_k/dL is constant with respect to k or L then the occurrence of the sequential STZs are independent, but if the occurrence of the current STZ is affected by past STZs or the load-path variable L, then dn_k/dL would change to reflect this. As is shown in the Appendix 2, the solution to eq. (6) is:

$$F_k(L) = \sum_{j=1}^{k} A_{k,j} \exp\left[-n_j(L)\,\Omega\right] \tag{7a}$$

where $A_{1,1}$=1, and the other $A_{k,j}$ are given recursively by

$$A_{k,j} = \frac{n'_k}{n'_k - n'_j} A_{k-1,j}, \text{ for all } j < k, n'_k = dn_k/dL, \text{ and } \sum_{j=1}^{k} A_{k,j} = 1. \tag{7b}$$

Next, we consider the likely form of the density of potential nuclei n_k. Quite generally, n_k may be written as:

$$n_k(\sigma) = f_k(\sigma)\exp[-(E - \Delta E)/k_B T] \tag{8a}$$

where $f_k(\sigma)$ is the dependence of n_k on the externally applied stress σ, $k_B T$ is the thermal energy, E is the activation energy for STZ formation, and ΔE is the increase in potential energy due to the accumulated strain from the previously operated STZs. The history effect shown in Fig. 5(d,e) is one in which previously operated STZs in the RVE raise the strain energy so that the formation of a new STZ from the RVE is enhanced. Therefore, ΔE is expected to increase as more STZs have formed and operated in the RVE, i.e. ΔE should be proportional to $(k-1)$. Eqn. (8a) can therefore be rewritten as:

$$n_k(\sigma) \propto \exp[\alpha_1(k-1)]\ f_k(\sigma) \tag{8b}$$

where α_1 is proportional to $1/k_B T$. Furthermore, $f_k(\sigma)$ may be assumed to be a power law σ^{m_k} in which the stress exponent (or Weibull modulus) m_k reflects the stress sensitivity of the operation of the k^{th} STZ. To model the possible effect that structural change due to the previously operated STZs may have on the stress sensitivity of the generation of a new STZ, m_k may increase or decrease as k increases, and a convenient form is $m_k \propto \exp[\alpha_2(k-1)]$ where α_2 can be positive or negative. Thus, we study the following phenomenological law for the STZ nucleus density:

$$n_k(\sigma) = \nu_k\, \sigma^{m_k} \tag{9}$$

where

$$\nu_k = \nu_1 \exp[\alpha_1(k-1)], \tag{10}$$

and

$$m_k = m_1 \exp[\alpha_2(k-1)] \tag{11}$$

Here, ν_1 and m_1 are positive model parameters, and the other two model parameters α_1 and α_2 control whether the nucleus density n_k grows or decays on increasing STZ order k. This simple model enables us to understand strain localization, which is a condition for shear band formation leading to yield or even shear fracture. As shown in the example in Fig. 7(a), when $\alpha_1, \alpha_2 > 0$, n_k in eqn. (9) grows rapidly with k, and the $F_k(\sigma)$ curves for successive k values calculated from eqn. (7) converge to an asymptotic behavior. In this case, successive occurrence of STZs in the same RVE Ω speeds up on increasing stress, and this may be regarded as the condition of shear localization that leads to a localized shear band. On the other hand, for $\alpha_1, \alpha_2 < 0$, the example in

Fig. 7(b) shows that the $F_k(\sigma)$ curves do not converge on increasing k, meaning that, at the same location, successive occurrence of STZs does not accelerate or even slows down. In this case, strain will not be localized. Physically, the model parameters α_1 and α_2 describe whether, and how fast, new STZs emerge due to a history or memory effect in the BMG microstructure after old STZs have operated in the same location. If past shear events generate new STZs, then the emergence rate of STZs will increase with k, and this will be the case represented by $\alpha_1, \alpha_2 > 0$. This should be the condition for shear localization that leads to shear banding. Also shown in Fig. 7(a) are the sum of the nucleus densities $n = \sum_{j=1}^{k} n_j$ and its emergence rate $dn/d\sigma$ in the asymptotic limit $k \to \infty$, after normalization by their maximum values. It can be seen that the emergence rate of STZ nuclei peaks at a stress of ~2GPa, which may be taken to be the average stress for shear band formation in this example. For stresses larger than this value, the survival probability drops to zero, and the nucleus density of STZs rises to a maximum, indicating the rapid acceleration of STZ emergence at high stresses.

Specifically, in the assumed growth law for the STZ nuclei in eqn. (10) and (11), α_1 reflects the interaction effects of nearby STZs (i.e. how the emergence of a new STZ is assisted by the stress field of a previous one nearby), α_2 reflects effects on the stress sensitivity or Weibull modulus due to previous STZs nearby (i.e. how the stress sensitivity of the nucleation of a new STZ is correlated with previous ones). The coupling effects of the two parameters α_1 and α_2 on strain localization or shear band formation are shown as in Fig. 8. The stress $\sigma_{0.5}$ at which $F_k(\sigma)$ = 0.5 for the k^{th} STZ is recorded, then the slope of the $\sigma_{0.5}$ vs k curve, i.e. $d\sigma_{0.5}/dk$, is calculated and plotted. If $d\sigma_{0.5}/dk$ approaches zero, then the $F_k(\sigma)$ curves finally converge at increasing k, implying the occurrence of shear localization; otherwise successive occurrence of STZs does not accelerate or even slows down on increasing k. It can be seen that changes in α_2 affect the occurrence of shear localization much more than changes in α_1.

What does the model tell – When the curves $F_k(\sigma)$ converge as $\rightarrow \infty$, the value $[1 - F_\infty(\sigma)]$ gives the fraction of the RVEs in the ensemble (i.e. the wire) that contain an infinite number of operated STZs and hence extreme straining, at different applied stress σ. Thus, in the example of Fig. 7(a), at $\sigma = 1$ GPa about half of the ensemble RVEs should have no STZ operated ($F_1 \approx 0.5$), about 20% of the RVEs should have two or more STZs operated ($F_2 \approx 0.8$), and only about 2% of the RVEs have extreme straining ($F_\infty \approx 0.98$). Therefore, at $\sigma = 1$ GPa, although the wire should have yielded, the overall plastic strain should be very small and extreme straining has not yet occurred. It will be seen that at $\sigma = 2$ GPa, about 45% of the RVEs have extreme straining ($F_\infty \approx 0.55$), while ~40% of the RVEs have not had the 5th STZ emerged ($F_5 \approx 0.4$) – this indicates exactly the situation of strain localization or shear banding, i.e. some locations in the sample have extreme straining while others have low strains. In the example of Fig. 7(a), the stress regime in which strain localization or shear banding occurs is approximately from 1.5 GPa to 2.5 GPa. At a much higher stress of 3 GPa, for example, nearly all of the RVEs have extreme straining ($F_\infty \approx 0.03$), and so straining becomes homogeneous again albeit extreme everywhere. However, shear fracture should have occurred beforehand in the stress window from ~1.5 GPa to 2.5 GPa where there is already a good chance that straining in some locations (RVEs) is already extreme.

Shear fracture condition – Therefore, shear fracture of the macroscopic wire occurs when shear banding in some of the RVEs in the ensemble become extreme, thus reaching a critical condition of instability. The survivability for the specimen against this would be represented by the $F_\infty(\sigma)$ curve for the average RVE in the ensemble.

First yield condition – As mentioned above, macroscopic yield of the wire at observable strain is not caused by the operation of the first STZ in the wire, but due to the operation of many isolated STZs in the wire, the average strain of which corresponds to the macroscopic proof strain. Therefore, assuming that all STZs produce the same shear, the condition of a given macroscopic proof strain would manifest itself as requiring an average RVE in the ensemble to have a certain number k_Ω of STZs already operated, so that the $F_{k_\Omega}(\sigma)$ curve for the ensemble RVEs (of small volume Ω) would represent the survivability $F(\sigma)$ of the macroscopic specimen against observable yield. As shown in Appendix 3, the number k_Ω of STZs needed per RVE to produce a macroscopic proof strain ε_y is given by

$$k_\Omega = \varepsilon_y \, (\lambda/s) \tag{12}$$

where λ is the length of each RVE, and s is the shear displacement produced by each STZ.

5. Reconciliation of MD and Experimental Results

MD results – Next, we use eqn. (7) to analyze the survival probabilities F_k calculated from the MD simulation results, in order to verify the reasonableness of the phenomenological growth law for the n_k in eqns. (9-11). To do this, the cuboid glassy simulation block was divided into 20 adjoining but non-overlapping RVEs, as shown in Fig. 9(a). Then, the stresses σ at which successive STZs occur in each RVE were recorded from a sequence of simulation snapshots. In order to increase the number of data for better statistical accuracy, the simulation was re-run with another randomly generated glassy block of the same dimensions and loading conditions, and the results were merged with the first set of simulation to obtain an ensemble of 40 RVE replicas. Amongst the 40 RVEs, the occurrence stresses σ_k for the k^{th} STZ were ranked, and the survival probability was calculated as $F_k(\sigma_k) = 1 - i/(N+1)$, where N = 40 is the total number of RVEs, and i is the rank of each σ_k in ascending order in the ensemble. The discrete data points in Fig. 9(b) show the calculated $F_k(\sigma)$ – it can be seen that, on increasing STZ order k, the F_k curves quickly approach an asymptotic state. This means that, as the applied stress is increased, the emergence and operation of successive STZs within a RVE speeds up quickly, thus indicating a strain localization behavior similar to Fig. 7(a). The model constitutive law in eqns. (9) to (11) can now be used to reconcile the MD results in Fig. 9(b). With such a law for n_k, the $F_k(\sigma)$ relations calculated from eqn. (7) are plotted in Fig. 9(b) as smooth curves. It can be seen that, by choosing $\alpha_1 = 0, \alpha_2 = 0.00275$, the predictions from eqn. (7) match the MD results rather well, thus showing the validity of eqns. (9-11) as a phenomenological law for n_k.

Experimental results – Next, we employ the above model to reconcile the experimental results in Fig. 4. Before this can be done, a reasonable value for the representative volume Ω needs to be assigned. As discussed in Section 3 above, the Ω in eqn. (7) should be the volume occupied by an eventual shear band that runs through the specimen thickness, plus some of its neighborhood, and since a shear band is likely to incline at 45° from the wire axis, Ω should be approximately a segment of the wire with length equal to the wire diameter. Moreover, according to the SEM observations in Fig. 2, shear bands are often intensively concentrated within segments of the BMG wires that are 50 μm long, regardless of the total gage length of the microwires. The length of 50 μm here is also close to the diameter (~45 μm) of the micro-wires. Hence, the magnitude Ω of the RVE is taken to be that of wire cylinder of length 45μm, i.e. $\Omega = 71.6 \times 10^3\ \mu\mathrm{m}^3$.

When using the survival probability curves $F_k(\sigma)$ from eqns. (7) to (11) to predict the experimental data of the $Cu_{48}Zr_{48}Al_4$ MG microwires, a caveat here is that for the first yield noticeable experimentally, the average quantity of STZs already operated in an RVE volume Ω in the sample is not known precisely, since yielding is a gradual process and the number of STZs operated should depend on the proof strain that is noticeable. However, yielding in metallic glasses should be just before shear banding, while fracture should be the state where shear banding is intense (Greer et al., 2013). Therefore, the process from the emergence of the first few STZs in an average RVE in the ensemble (e.g. snapshot 1 in Fig. 5(b)), to the clear-cut formation of shear banding (e.g. snapshot 7 in Fig. 5(b)), may be taken to represent the strain path from first yield to fracture. For a given macroscopic proof strain ε_y, the number k_Ω of STZs needed in an average RVE is given by eqn. (12) (see Appendix 3). Fig. 1 indicates that for the present microwire samples, the proof strain at noticeable yield should be on the order of $\varepsilon_y \sim 0.001$. As stated above, the length λ of each RVE is close to the wire diameter which is ~ 45 μm. Considering that the shear displacement s of each STZ is likely to be on the order of a few nm's, the k_Ω estimated from eqn. (12) is on the order of 10. Also, as discussed above, the survivability of the sample against fracture should be represented by the $F_\infty(\sigma)$ curve for the average RVE in the ensemble. Fig. 10(a-c) show the predicted $F_k(\sigma)$ curves on increasing event order k obtained from eqns. (7) to (11) for a set of model parameters, alongside with the experimental data for the survivability against first yield and fracture for the present $Cu_{48}Zr_{48}Al_4$ MG microwires shown in Fig. 4. It can be seen that the model parameters are chosen such that the $F_\infty(\sigma)$ curve matches the experimental fracture data, whereas the $F_{10}(\sigma)$ curve matches the experimental first yield data. Here, the value of 10 for k_Ω here is only an order-of-magnitude estimate, but one can see that the model can capture the transition from first yield to fracture in at least an indicative way.

6. Discussion

The major significance of the present work falls in the following three aspects:

(i) MD simulations elucidate clearly how shear bands are formed from the correlated operation of STZs. Although glass plasticity is widely believed to take place via STZs, STZs are atomic-scale clusters and how they lead to microscopic shear banding remains poorly understood. The present MD simulations in Figs. 5 and 7 show, for the first time, that shear bands are formed from the correlated emergence and operation of STZs in a cascade manner. Before the occurrence of shear banding (e.g. snapshots 1 to 2 in Fig. 5(b)), the glassy plasticity is due to the uncorrelated emergence and operation of isolated STZs in the sample, and such a deformation mode is homogeneous without strain localization. Then, due to a history effect where new STZs preferentially emerge in the high stress regions close to previously operated STZs (Fig. 5(e)), the emergence of STZs becomes correlated in both the time and space domains (Fig. 5(d)).

(ii) A novel statistical-ensemble model (eqns. 6-7) was constructed to describe the stochastic nature of shear banding in glasses, as described in Section 4. This model is based on statistical mechanics consideration of an ensemble of micro-scale RVEs which are potent to undergo shear banding. The input to this model is a growth law for the STZ nuclei density along the strain path (eqns. 9-11), and the model predicts whether shear localization will occur (Fig. 8), and if it does, the occurrence probability (Fig. 7(a), as an example). By choosing suitable parameters for the growth law, the model can capture the MD and experimental results well (Figs. 9(b) and 10). In particular, the model can describe the history effect in (i) above, namely, the notion that previous operated STZs trigger the occurrence of new STZs nearby is described by an accelerated growth law for the STZ nuclei density illustrated in eqns. (9-11) and Fig. 8. The severity of the history effect, which dictates the potential of the glass to undergo shear banding, is represented mainly by the parameter α_2 (Fig. 8) which reflects how rapidly the stress sensitivity of STZ nucleation (m_k) grows due to the operation of past STZs nearby (eqns. 9 and 11). Although the growth law in eqns. (9-11) is phenomenological, it provides the first mathematical description for the intrinsic process of shear banding in glasses from correlated STZ generation.

(iii) The present experimental results in Figs. 1, 3 and 4 show clearly the length independence of strength of the glass wires studied. While this may be counter-intuitive for some readers, to the best knowledge of the present authors there has not been any report proving that glass microwires exhibit an obvious length dependence on strength. On the contrary, Pardini and Manhani (Pardini and Manhani, 2002) tested carbon and glass fibers and reported strength data that do not vary with the fiber length in a statistically significant way. Furthermore, their $\ln\ln(1/F)$ vs $\ln\sigma_f$ plots also collapse into straight-line trends regardless of the fiber length, in a similar way as Fig. 4 and according to eqn. (2). For high-quality fibers, that strength should be independent of length is in fact well expected from the discussion in Section 3, namely, that yield or fracture is controlled by the average or extreme behavior of many simultaneous STZs or shear bands in different locations in the wire. The nuclei or volume elements that are pertinent to their emergence are small and isolated, and they form a statistical ensemble in thermo-mechanical equilibrium. It is then a simple fact in statistical mechanics that the size of the ensemble, which is the volume of the wire, does not affect the distribution, or average or extreme behavior in the ensemble.

While the present MD simulations in Fig. 5 elucidate the process of shear banding, it is also important to realize their limitations. It can be noted that the Weibull modulus m_1 from the

MD simulations in Fig. 9(b) is ~27.98, while that for first yield in the experiments ranges from 2.17 to 2.52 in Fig. 4. In fact, the RVE of $\Omega = 71.6 \times 10^3\ \mu\text{m}^3$ in the real experiments is around ~10^{11} times of that in MD simulations, and the deformation time scale is also many magnitudes longer, thus the MD simulated glassy structures should be much less varying than the real experimental samples. A more monolithic ensemble should have a larger Weibull modulus and this should explain the discrepancy between the MD and experimental values. Noteworthily, Weibull moduli much larger than the present were reported in some previous experiments (Neilson et al., 2015; Wu et al., 2010; Zhang et al., 2016). However, in such experiments, tensile samples which failed at the gripped points were not excluded from the analysis, or compressive loading was used which suppressed the propagation of stick-slip shear bands in MG specimens. In the present experiments, as stated in Section 2, those tensile micro-wire specimens that broke at the gripped ends were excluded from the analysis, and so it is reasonable for the Weibull modulus to be lower; in fact the present Weibull moduli should reflect the intrinsic behavior of the materials rather than effects due to stress concentration at the gripped ends.

Finally, a note on the effects of cross-sectional areas of the experimental micro-wires is also necessary. As stated in Section 2 above, the micro-wires used in the present experiments were very uniform in cross-section to begin with, and wires with non-uniform cross sections were discarded. In Fig. 4, the Weibull model is applied to both the first-yield and fracture strength. Up to the first-yield strength, the deformation is elastic and uniform, and so Weibull modelling should be very valid. For the fracture, somewhere the cross-section will be reduced when slip bands have occurred, although for places without slip bands the cross section did not change significantly, as observed in Fig. 2(c). Such local cross-sectional area changes are not explicitly modelled in the Weibull model. However, in the MD simulations in Figs. 5 and 9, the RVEs are arranged periodically, so there are no free surfaces or any local cross-sectional area changes. Fig. 9(b) still shows that the MD simulated results also exhibit accelerated and correlated STZ occurrence that agrees well with predictions from the Weibull model. In a real micro-wire undergoing shear localization, additional complications would arise due to the cross-sectional area reductions locally, but when this happens, one can just expect the acceleration of the correlated STZ emergence, and hence the localized shear, to be even faster. The main physics unveiled here is still the correlated STZs and their accelerated occurrence, while the local areal changes towards the fracture are relatively unimportantly conceptually.

7. Conclusion

To conclude, a stochastic model was proposed to describe strain localization leading to shear fracture in BMGs. The model predicts that, if the intrinsic emergence rate of the shear transformation zones grows along the strain path, then the successive occurrence of discrete shear events speeds up rapidly leading to shear localization in the form of a shear band. MD simulations indicated strong correlation of the occurrence of discrete shear events and their exponential growth along the strain path. The model gives predictions that agree well with experimental results from three kinds of Cu/Zr-based BMG microwires.

Acknowledgements

The work described in this paper is supported by funding from the Kingboard Professorship Endowment and the National Natural Science Foundation of China (Grant Nos 51671070 and 51671071).

References

Albe, K., Ritter, Y., Şopu, D., 2013. Enhancing the plasticity of metallic glasses: Shear band formation, nanocomposites and nanoglasses investigated by molecular dynamics simulations. Mechanics of Materials 67, 94-103.

Argon, A., 1979. Plastic deformation in metallic glasses. Acta Metall 27, 47-58.

Bletry, M., Guyot, P., Blandin, J.J., Soubeyroux, J.L., 2006. Free volume model: High-temperature deformation of a Zr-based bulk metallic glass. Acta Mater. 54, 1257-1263.

Carroll, J.D., Brewer, L.N., Battaile, C.C., Boyce, B.L., Emery, J.M., 2012. The effect of grain size on local deformation near a void-like stress concentration. Int. J. Plasticity 39, 46-60.

Chen, X.X., Ngan, A.H.W., 2012. Tensile deformation of silver micro-wires of small thickness-to-grain-size ratios. Mat. Sci. Eng. A 539, 74-84.

Cheng, Y.Q., Ma, E., Sheng, H.W., 2009. Atomic level structure in multicomponent bulk metallic glass. Phys Rev Lett 102, 245501.

Chung, K., Lee, C., Kim, H., 2014. Forming limit criterion for ductile anisotropic sheets as a material property and its deformation path insensitivity, Part II: Boundary value problems. Int. J. Plasticity 58, 35-65.

Ding, J., Patinet, S., Falk, M.L., Cheng, Y., Ma, E., 2014. Soft spots and their structural signature in a metallic glass. Proceedings of the National Academy of Sciences 111, 14052-14056.

Fornell, J., Concustell, A., Suriñach, S., Li, W.H., Cuadrado, N., Gebert, A., Baró, M.D., Sort, J., 2009. Yielding and intrinsic plasticity of Ti–Zr–Ni–Cu–Be bulk metallic glass. Int. J. Plasticity 25, 1540-1559.

Greer, A.L., Cheng, Y.Q., Ma, E., 2013. Shear bands in metallic glasses. Materials Science and Engineering: R: Reports 74, 71-132.

Guo, H., Yan, P., Wang, Y., Tan, J., Zhang, Z., Sui, M., Ma, E., 2007a. Tensile ductility and necking of metallic glass. Nature materials 6, 735.

Guo, H., Yan, P.F., Wang, Y.B., Tan, J., Zhang, Z.F., Sui, M.L., Ma, E., 2007b. Tensile ductility and necking of metallic glass. Nature materials 6, 735-739.

Huespe, A.E., Needleman, A., Oliver, J., Sánchez, P.J., 2012. A finite strain, finite band method for modeling ductile fracture. Int. J. Plasticity 28, 53-69.

Ibnabdeljalil, M., Curtin, W., 1997. Strength and reliability of fiber-reinforced composites: localized load-sharing and associated size effects. International Journal of Solids and Structures 34, 2649-2668.

Jang, D., Greer, J.R., 2010. Transition from a strong-yet-brittle to a stronger-and-ductile state by size reduction of metallic glasses. Nature materials 9, 215.

Jang, D., Gross, C.T., Greer, J.R., 2011. Effects of size on the strength and deformation mechanism in Zr-based metallic glasses. Int. J. Plasticity 27, 858-867.

Jiang, S.-S., Huang, Y.-J., Wu, F.-F., Xue, P., Sun, J.-F., 2018. A CuZr-based bulk metallic glass composite with excellent mechanical properties by optimizing microstructure. Journal of Non-Crystalline Solids 483, 94-98.

Kaban, I., Jóvári, P., Escher, B., Tran, D.T., Svensson, G., Webb, M.A., Regier, T.Z., Kokotin, V., Beuneu, B., Gemming, T., Eckert, J., 2015. Atomic structure and formation of CuZrAl bulk metallic glasses and composites. Acta Mater. 100, 369-376.

Klaumünzer, D., Maaß, R., Löffler, J.F., 2011. Stick-slip dynamics and recent insights into shear banding in metallic glasses. J. Mater. Res. 26, 1453-1463.

Liu, J.W., Cao, Q.P., Chen, L.Y., Wang, X.D., Jiang, J.Z., 2010. Shear band evolution and hardness change in cold-rolled bulk metallic glasses. Acta Mater. 58, 4827-4840.

Liu, Y.H., Wang, G., Wang, R.J., Zhao, D.Q., Pan, M.X., Wang, W.H., 2007. Super Plastic Bulk Metallic Glasses at Room Temperature. Science 315, 1385-1388.

Lu, J., Ravichandran, G., Johnson, W.L., 2003. Deformation behavior of the $Zr_{41.2}Ti_{13.8}Cu_{12.5}Ni_{10}Be_{22.5}$ bulk metallic glass over a wide range of strain-rates and temperatures. Acta Mater. 51, 3429-3443.

Luan, Y.W., Li, C.H., Han, X.J., Li, J.G., 2017. Plastic deformation behaviours of CuZr amorphous/crystalline nanolaminate: a molecular dynamics study. Molecular Simulation 43, 1116-1124.

Maaß, R., Löffler, J.F., 2015. Shear-Band Dynamics in Metallic Glasses. Advanced Functional Materials 25, 2353-2368.

Neilson, H.J., Petersen, A.S., Cheung, A.M., Poon, S.J., Shiflet, G.J., Widom, M., Lewandowski, J.J., 2015. Weibull modulus of hardness, bend strength, and tensile strength of Ni−Ta−Co−X metallic glass ribbons. Mat. Sci. Eng. A 634, 176-182.

Ngan, A.H.W., 2009. Canonical ensemble for static elastic structures with random microstructures. J. Mech. Phys. Solids. 57, 803-811.

Ngan, A.H.W., Ng, K.S., 2010. Transition from deterministic to stochastic deformation. Phil. Mag. 90, 1937-1954.

Pardini, L.C., Manhani, L.G.B., 2002. Influence of the testing gage length on the strength, Young's modulus and Weibull modulus of carbon fibres and glass fibres. Materials research 5, 411-420.

Phoenix, S., Raj, R., 1992. Overview no. 100 Scalings in fracture probabilities for a brittle matrix fiber composite. Acta metallurgica et materialia 40, 2813-2828.

Plimpton, S., 1995. Fast parallel algorithms for short-range molecular dynamics. Journal of computational physics 117, 1-19.

Pugno, N.M., Ruoff, R.S., 2006. Nanoscale Weibull statistics. J. Appl. Phys 99, 024301.

Qin, F.X., Bingham, N.S., Wang, H., Peng, H.X., Sun, J.F., Franco, V., Yu, S.C., Srikanth, H., Phan, M.H., 2013. Mechanical and magnetocaloric properties of Gd-based amorphous microwires fabricated by melt-extraction. Acta Mater. 61, 1284-1293.

Ramamurty, U., Jana, S., Kawamura, Y., Chattopadhyay, K., 2005. Hardness and plastic deformation in a bulk metallic glass. Acta Mater. 53, 705-717.

Schuh, C., Hufnagel, T., Ramamurty, U., 2007. Mechanical behavior of amorphous alloys. Acta Mater. 55, 4067-4109.

Sha, Z.D., He, L.C., Xu, S., Pei, Q.X., Liu, Z.S., Zhang, Y.W., Wang, T.J., 2014. Effect of aspect ratio on the mechanical properties of metallic glasses. Scripta Mater. 93, 36-39.

Shen, H., Wang, H., Jingshun, L., Cao, F., Qin, F., Xing, D., Chen, D., Liu, Y., Sun, J., 2014a. Enhanced magnetocaloric properties of melt-extracted GdAlCo metallic glass microwires. Journal of Magnetism and Magnetic Materials 372, 23-26.

Shen, H., Wang, H., Liu, J., Xing, D., Qin, F., Cao, F., Chen, D., Liu, Y., Sun, J., 2014b. Enhanced magnetocaloric and mechanical properties of melt-extracted Gd55Al25Co20 micro-fibers. Journal of Alloys and Compounds 603, 167-171.

Shimizu, F., Ogata, S., Li, J., 2006. Yield point of metallic glass. Acta Mater. 54, 4293-4298.

Shimizu, F., Ogata, S., Li, J., 2007. Theory of shear banding in metallic glasses and molecular dynamics calculations. Materials transactions 48, 2923-2927.

Sopu, D., Foroughi, A., Stoica, M., Eckert, J., 2016. Brittle-to-Ductile Transition in Metallic Glass Nanowires. Nano letters 16, 4467-4471.

Şopu, D., Ritter, Y., Gleiter, H., Albe, K., 2011. Deformation behavior of bulk and nanostructured metallic glasses studied via molecular dynamics simulations. Physical Review B 83.

Şopu, D., Stoica, M., Eckert, J., 2015. Deformation behavior of metallic glass composites reinforced with shape memory nanowires studied via molecular dynamics simulations. Applied Physics Letters 106, 211902.

Şopu, D., Stukowski, A., Stoica, M., Scudino, S., 2017. Atomic-Level Processes of Shear Band Nucleation in Metallic Glasses. Phys Rev Lett 119, 195503.

Sun, X., Choi, K.S., Liu, W.N., Khaleel, M.A., 2009. Predicting failure modes and ductility of dual phase steels using plastic strain localization. Int. J. Plasticity 25, 1888-1909.

Weibull, W., 1951. A statistical distribution function of wide applicability. Journal of applied mechanics 18, 293-297.

Wu, W.F., Li, Y., Schuh, C.A., 2008. Strength, plasticity and brittleness of bulk metallic glasses under compression: statistical and geometric effects. Phil. Mag. 88, 71-89.

Wu, Y., Bei, H., Wang, Y.L., Lu, Z.P., George, E.P., Gao, Y.F., 2015. Deformation-induced spatiotemporal fluctuation, evolution and localization of strain fields in a bulk metallic glass. Int. J. Plasticity 71, 136-145.

Wu, Y., Wu, H.H., Hui, X.D., Chen, G.L., Lu, Z.P., 2010. Effects of drawing on the tensile fracture strength and its reliability of small-sized metallic glasses. Acta Mater. 58, 2564-2576.

Xu, B., Falk, M.L., Li, J.F., Kong, L.T., 2018. Predicting Shear Transformation Events in Metallic Glasses. Phys Rev Lett 120, 125503.

Xu, Y.K., Ma, H., Xu, J., Ma, E., 2005. Mg-based bulk metallic glass composites with plasticity and gigapascal strength. Acta Mater. 53, 1857-1866.

Yoo, B.G., Kim, J.Y., Kim, Y.J., Choi, I.C., Shim, S., Tsui, T.Y., Bei, H., Ramamurty, U., Jang, J.i., 2012. Increased time-dependent room temperature plasticity in metallic glass nanopillars and its size-dependency. Int. J. Plasticity 37, 108-118.

Zhang, J., Estévez, D., Zhao, Y.-Y., Huo, L., Chang, C., Wang, X., Li, R.-W., 2016. Flexural Strength and Weibull Analysis of Bulk Metallic Glasses. Journal of Materials Science & Technology 32, 129-133.

Zhao, P., Li, J., Wang, Y., 2013. Heterogeneously randomized STZ model of metallic glasses: Softening and extreme value statistics during deformation. Int. J. Plasticity 40, 1-22.

Zhao, Y.Y., Ma, E., Xu, J., 2008. Reliability of compressive fracture strength of Mg–Zn–Ca bulk metallic glasses: Flaw sensitivity and Weibull statistics. Scripta Mater. 58, 496-499.

Zhou, H., Qu, S., Yang, W., 2013. An atomistic investigation of structural evolution in metallic glass matrix composites. Int. J. Plasticity 44, 147-160.

Zhou, X., Zhou, H., Li, X., Chen, C., 2015. Size effects on tensile and compressive strengths in metallic glass nanowires. J. Mech. Phys. Solids. 84, 130-144.

Zhu, F., Hirata, A., Liu, P., Song, S., Tian, Y., Han, J., Fujita, T., Chen, M., 2017. Correlation between Local Structure Order and Spatial Heterogeneity in a Metallic Glass. Phys Rev Lett 119, 215501.

Appendix 1 – Glossary of Terms

BMG – bulk metallic glass

MG – metallic glass

PBC – periodic boundary conditions

RVE – representative volume element

STZ – shear transformation zone

F – survival probability (dimensionless)

F_k – ensemble survivability against the emergence of the kth STZ, i.e. fraction of ensemble replicas in which the kth STZ has not yet occurred (dimensionless)

k_Ω – number of STZs operated in an RVE needed to produce macroscopic yielding

L – a variable along the strain path

m – Weibull modulus (dimensionless)

m_k – stress sensitivity of STZ nuclei density n_k; a model parameter in eqns. (9, 11)

N – number of replicas in ensemble (ensemble size); number of samples tested

n_k – density of nuclei for the kth STZ, i.e. number of STZ nuclei per unit volume, averaged from all the RVEs in the ensemble

p – joint probability density of the spatial and temporal separation of the occurrence of two STZs

$\vec{r}_i$ – position of the ith STZ

Δr_{ij} – distance between the ith STZ and the jth STZ (nm)

s – shear displacement of each STZ (nm)

t_i – time at which the i^{th} STZ occurs (ps)

Δt_{ij} – difference in occurrence times of the i^{th} STZ and the j^{th} STZ (ps)

V – volume of specimen (mm^3)

α_1, α_2 – model parameters in eqns. (9-11)

ε – strain (dimensionless)

ε_y – macroscopic proof strain (dimensionless)

λ – length of RVE (μm)

ν_k – model parameter in eqns. (9, 10)

σ – tensile stress (MPa)

σ_0 – normalizing constant of stress unit in Weibull formula (MPa)

σ_f – fracture stress (MPa)

σ_y – yield stress (MPa)

Ω – volume of RVE (μm^3)

Appendix 2 – Proof of eqn. (7a,b)

Eqn. (6) reads

$$\frac{dF_k}{dL} + F_k\,(n_k'\Omega) = F_{k-1}(n_k'\Omega) \tag{A1}$$

where $n_k' = dn_k/dL$. This equation can be solved recursively. For $k = 1$, the $F_{k-1} = F_0$ on the right side is zero, and so the solution to eq. (A1) is $F_1(L) = \exp[-n_1(L)\Omega]$, which satisfies the form in eqn. (7a, b) in the main text. Next, we show eqn. (7) by induction. Given eqn. (7) is correct for $k-1$, we prove that it is also correct for k. We therefore seek a particular solution to

$$\frac{dF_k}{dL} + F_k\,(n_k'\Omega) = (n_k'\Omega)\sum_{j=1}^{k-1} A_{k-1,j}\exp\left[-n_j(L)\,\Omega\right] \tag{A2}$$

To satisfy the right side, the particular solution to eqn. (A2) has to take the form

$$F_k(\text{particular}) = \sum_{j=1}^{k-1} A_{k,j}\exp\left[-n_j(L)\,\Omega\right] \tag{A3}$$

where $A_{k,j}$, $j = 1, 2, \ldots, k-1$, are new constants to be found. Substituting eqn. (A3) into eqn. (A2), we find

$$A_{k,j} = \frac{n_k'}{n_k' - n_j'} A_{k-1,j} \tag{A4}$$

so that the first condition in eqn. (7b) in the main text is verified for the case of k. Furthermore, the homogeneous solution to eqn. (A2) is

$$F_k(\text{homogeneous}) = A_{k,k}\exp[-n_k(L)\,\Omega] \tag{A5}$$

where $A_{k,k}$ is a constant to be found. The full solution for F_k is therefore

$$F_k = F_k(\text{particular}) + F_k(\text{homogeneous}) = \sum_{j=1}^{k} A_{k,j}\exp\left[-n_j(L)\,\Omega\right] \tag{A6}$$

which is the form in eqn. (7a). Moreover, by the conditions $F_k(L = 0) = 1$ and $n_j(L = 0) = 0$, we have $\sum_{j=1}^{k} A_{k,j} = 1$ which allows the last constant $A_{k,k}$ to be found, given the other $A_{k,j}$ terms are known from eqn. (A4). Also, the second equation in eqn. (7b) in the main text is also verified for the case of k.

Appendix 3 – Eqn. (12)

The number k_Ω of STZs needed in each RVE to produce a macroscopic proof strain ε_y is estimated here. Assume that the shear displacements of the operated STZs add up to produce the overall elongation of the sample:

$$k_V\, s = \varepsilon_y\, (\mathrm{V/A}) \tag{A7}$$

where k_V is the total number of STZs already operated in the macroscopic sample (of volume V, and cross-sectional area A), s is the shear displacement of each STZ, ε_y is the macroscopic proof strain, and $\mathrm{V/A}$ is the length of the macroscopic sample. Suppose the STZs are rather homogeneously distributed, then $k_V/V = k_\Omega/\Omega$, and so eqn. (A7) becomes eqn. (12), in which $\lambda = \Omega/\mathrm{A}$ is the length of each of the RVEs, which are stacked together along the axis of the wire sample as shown in Fig. 6.

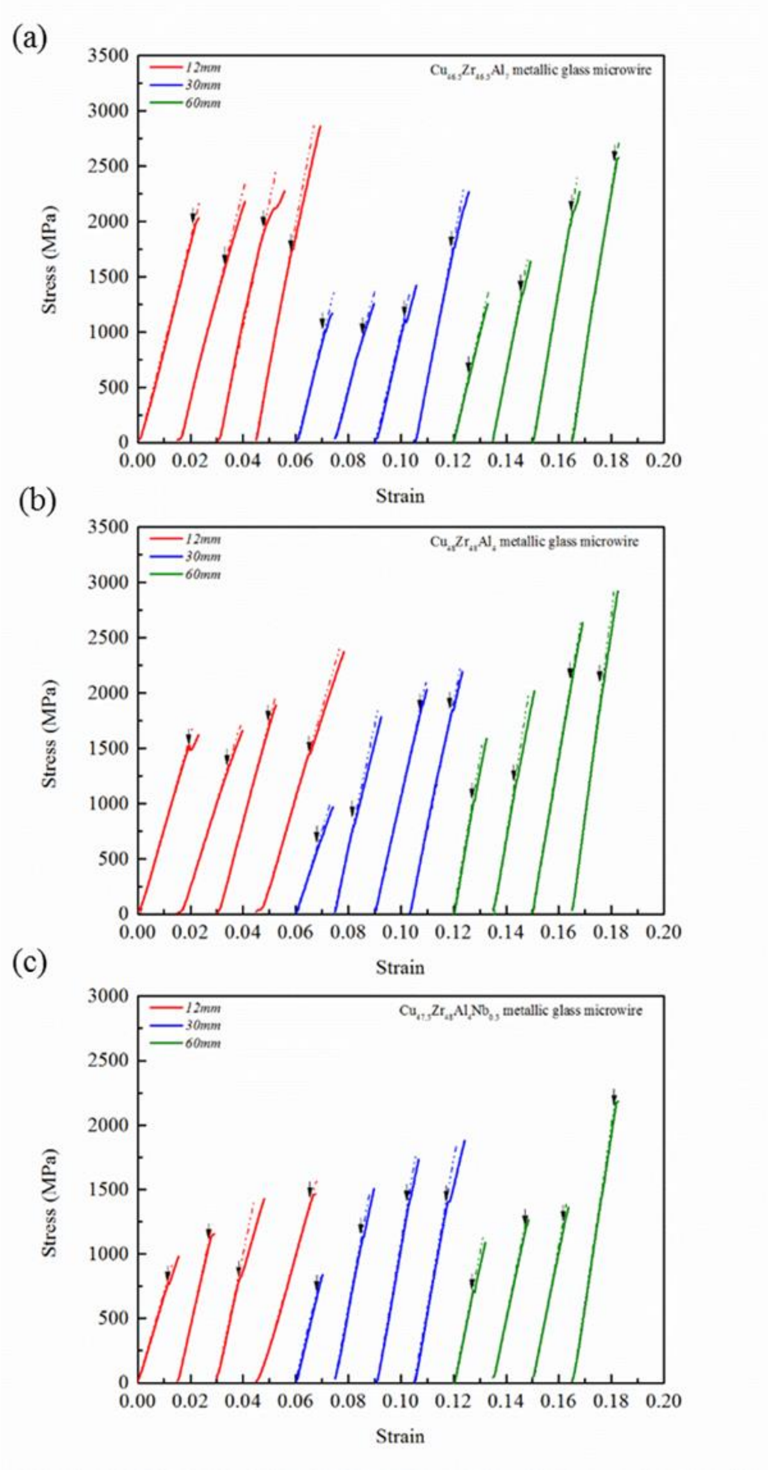

Figure 1. Typical strain-stress curves for (a) $Cu_{46.5}Zr_{46.5}Al_7$, (b) $Cu_{48}Zr_{48}Al_4$ and (c) $Cu_{47.5}Zr_{48}Al_4Nb_{0.5}$ microwires in tension. The incipient yielding point of shear band is indicated by black-color arrows.

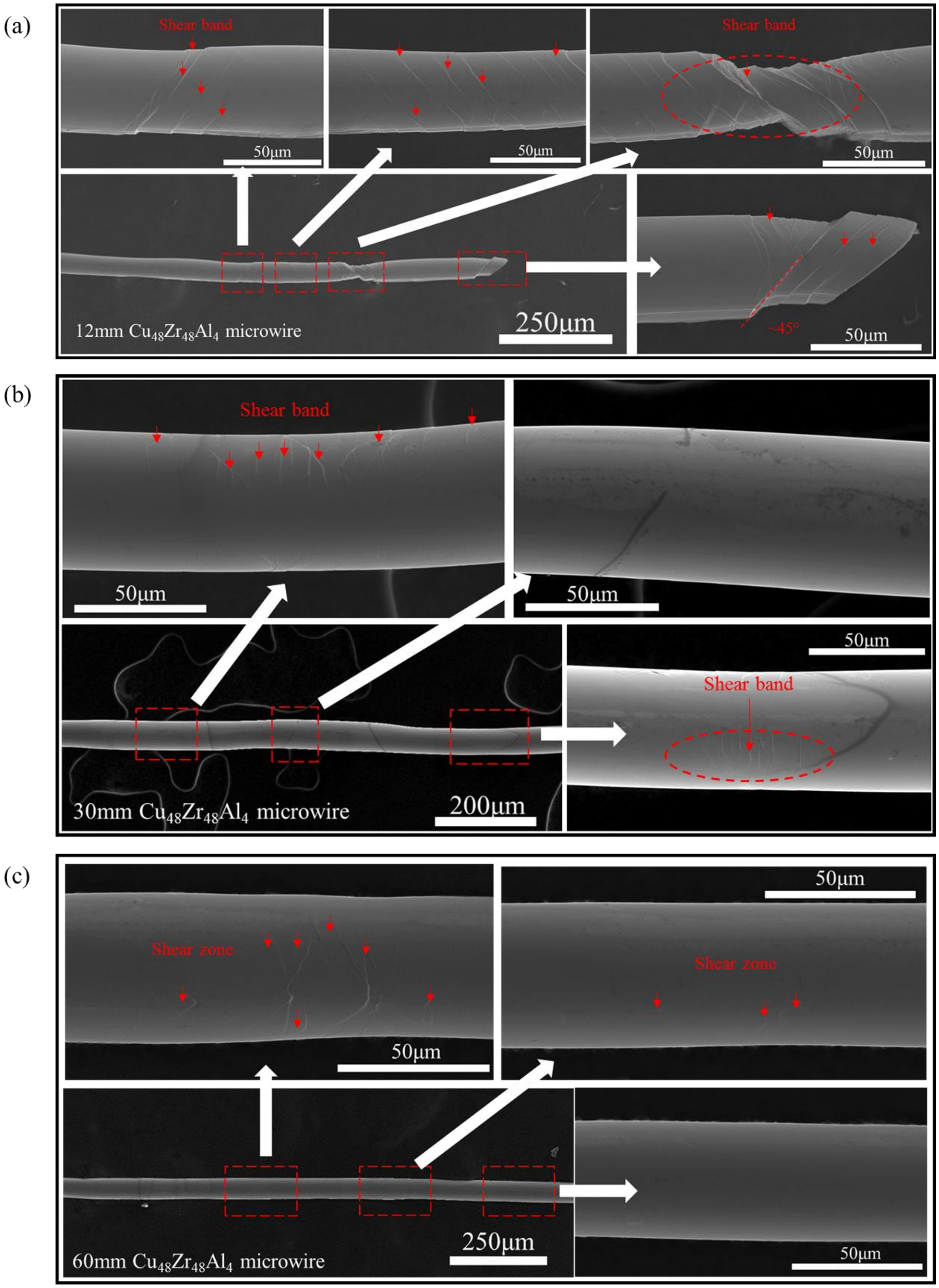

Figure 2. Typical SEM images of $Cu_{48}Zr_{48}Al_4$ with gauge lengths of (a) 12mm (b) 30mm and (c) 60mm after deformation. The occurrence of shear bands is marked by red arrows.

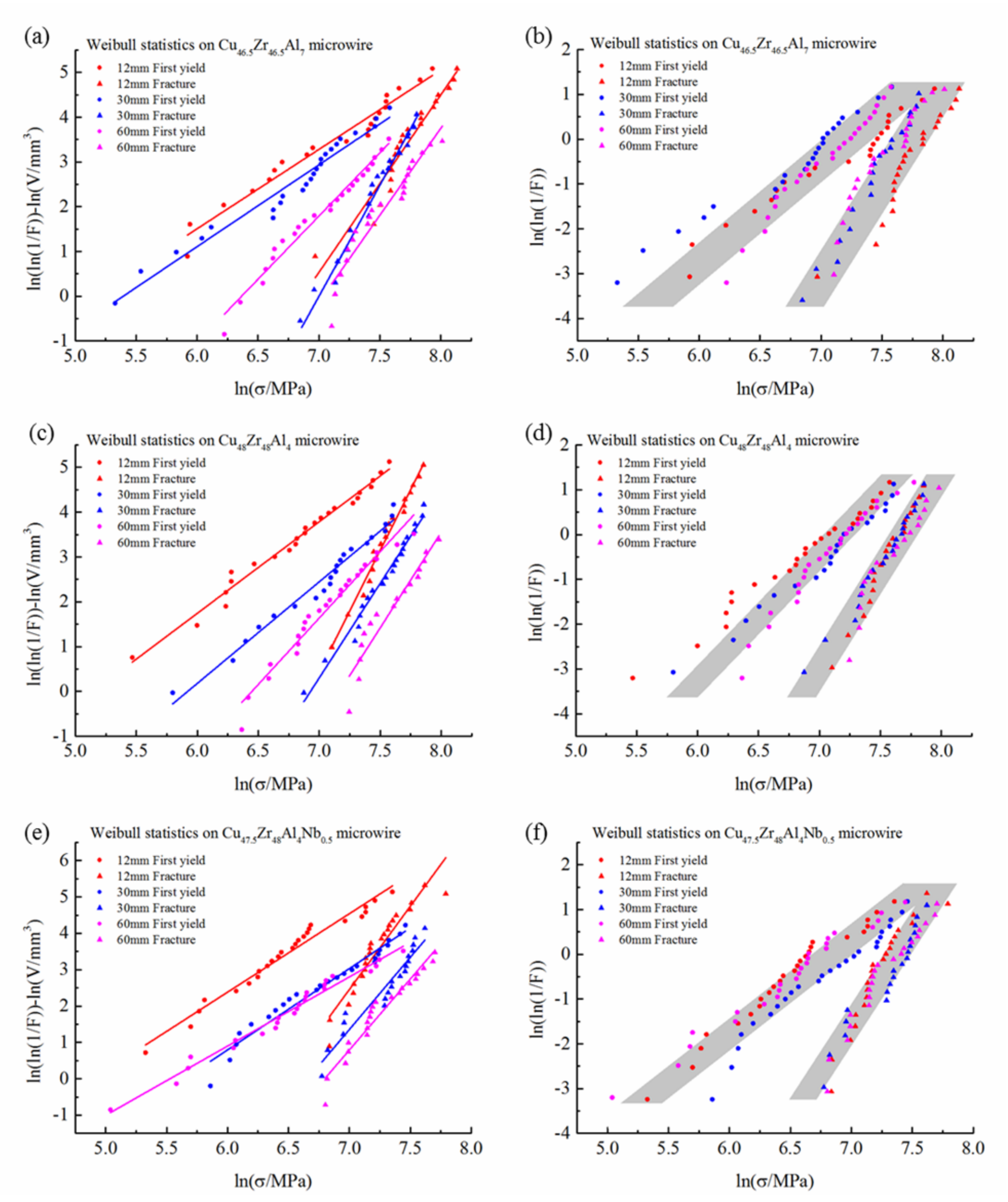
(a)
Weibull statistics on $Cu_{46.5}Zr_{46.5}Al_7$ microwire
12mm First yield
12mm Fracture
30mm First yield
30mm Fracture
60mm First yield
60mm Fracture
ln(ln(1/F))-ln(V/mm^3)
ln(σ/MPa)
(b)
Weibull statistics on $Cu_{46.5}Zr_{46.5}Al_7$ microwire
ln(ln(1/F))
ln(σ/MPa)
(c)
Weibull statistics on $Cu_{48}Zr_{48}Al_4$ microwire
ln(ln(1/F))-ln(V/mm^3)
ln(σ/MPa)
(d)
Weibull statistics on $Cu_{48}Zr_{48}Al_4$ microwire
ln(ln(1/F))
ln(σ/MPa)
(e)
Weibull statistics on $Cu_{47.5}Zr_{48}Al_4Nb_{0.5}$ microwire
ln(ln(1/F))-ln(V/mm^3)
ln(σ/MPa)
(f)
Weibull statistics on $Cu_{47.5}Zr_{48}Al_4Nb_{0.5}$ microwire
ln(ln(1/F))
ln(σ/MPa)

Figure 3. Weibull plots for first-yield and fracture strength of tested BMG microwires grouped according to their lengths: (a, b) $Cu_{46.5}Zr_{46.5}Al_7$, (c, d) $Cu_{48}Zr_{48}Al_4$ and (e,f) $Cu_{47.5}Zr_{48}Al_4Nb_{0.5}$. In (a, c, e), *V* is the volume of the micro-wire gauge length, which is proportional to the wire length as all wires have a common diameter of ~45μm.

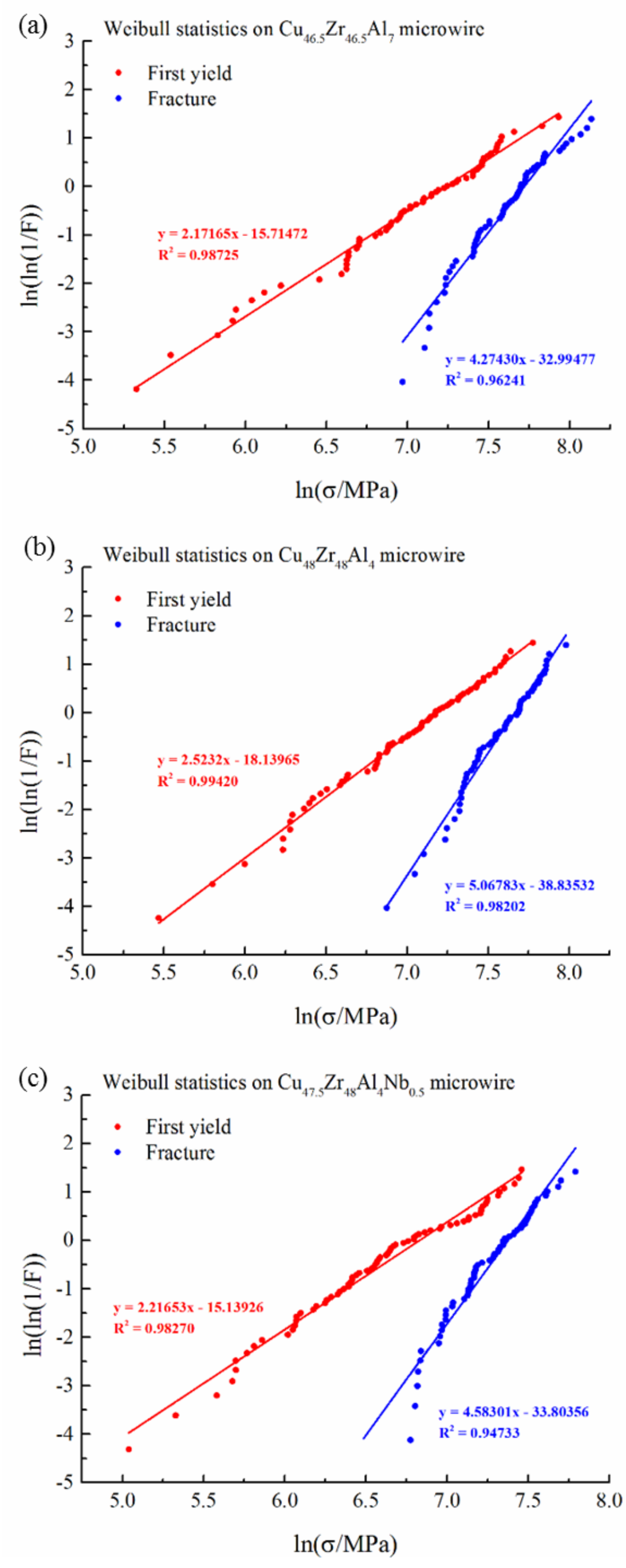

Figure 4. Weibull plots for first-yield and fracture strength of tested BMG microwires without referencing to their lengths: (a) $Cu_{46.5}Zr_{46.5}Al_7$, (b) $Cu_{48}Zr_{48}Al_4$ and (c) $Cu_{47.5}Zr_{48}Al_4Nb_{0.5}$.

(a)

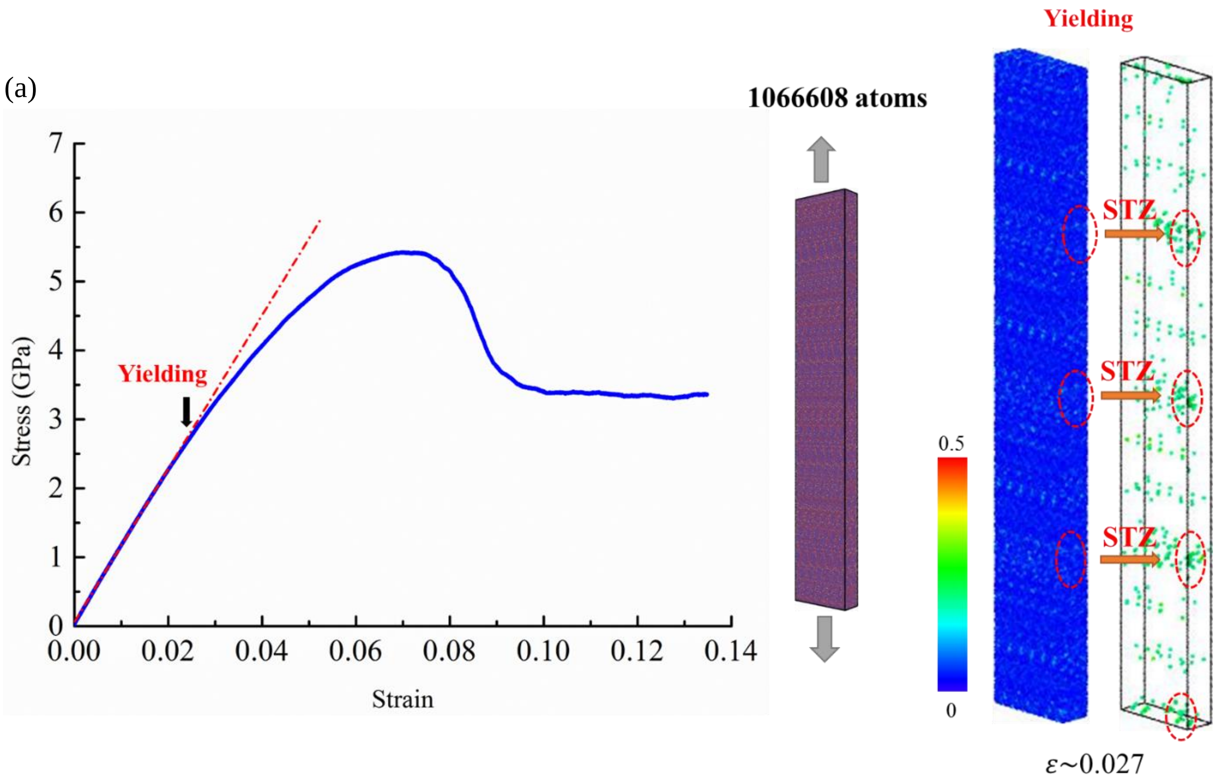
Stress (GPa)
0
1
2
3
4
5
6
7
0.00
0.02
0.04
0.06
0.08
0.10
0.12
0.14
Strain
Yielding
1066608 atoms
Yielding
STZ
STZ
STZ
0.5
0
ε~0.027

(b)

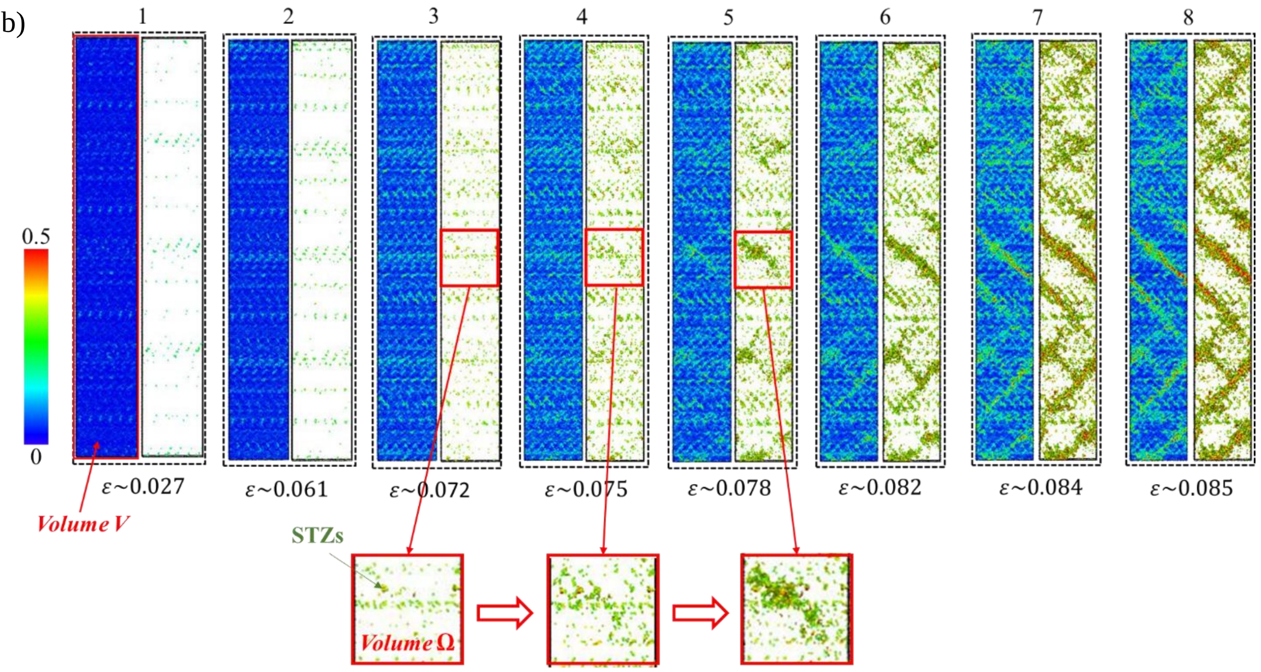
1
2
3
4
5
6
7
8
0.5
0
ε~0.027
ε~0.061
ε~0.072
ε~0.075
ε~0.078
ε~0.082
ε~0.084
ε~0.085
Volume V
STZs
Volume Ω

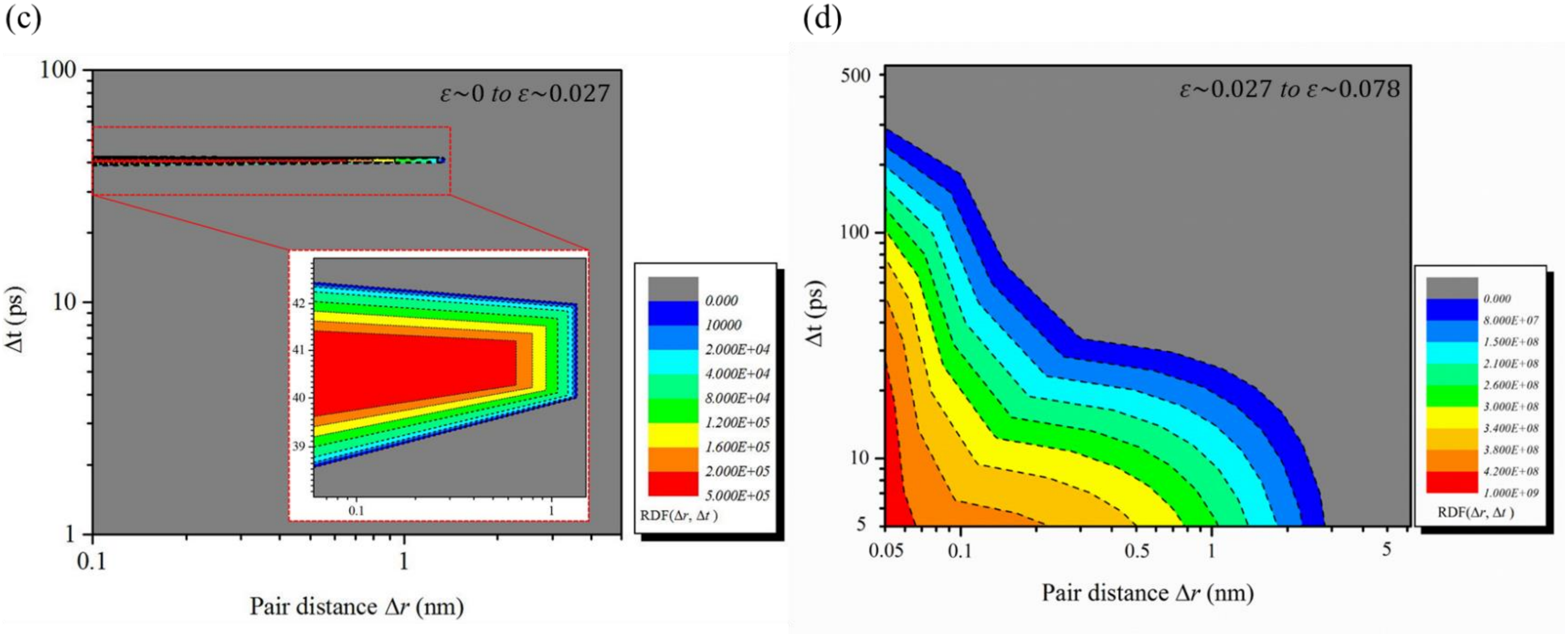
(c)
100
10
1
0.1
1
Δt (ps)
Pair distance Δr (nm)
ε~0 to ε~0.027
42
41
40
39
0.1
1
0.000
10000
2.000E+04
4.000E+04
8.000E+04
1.200E+05
1.600E+05
2.000E+05
5.000E+05
RDF(Δr, Δt)
(d)
500
100
10
5
0.05
0.1
0.5
1
5
Δt (ps)
Pair distance Δr (nm)
ε~0.027 to ε~0.078
0.000
8.000E+07
1.500E+08
2.100E+08
2.600E+08
3.000E+08
3.400E+08
3.800E+08
4.200E+08
1.000E+09
RDF(Δr, Δt)

(e)

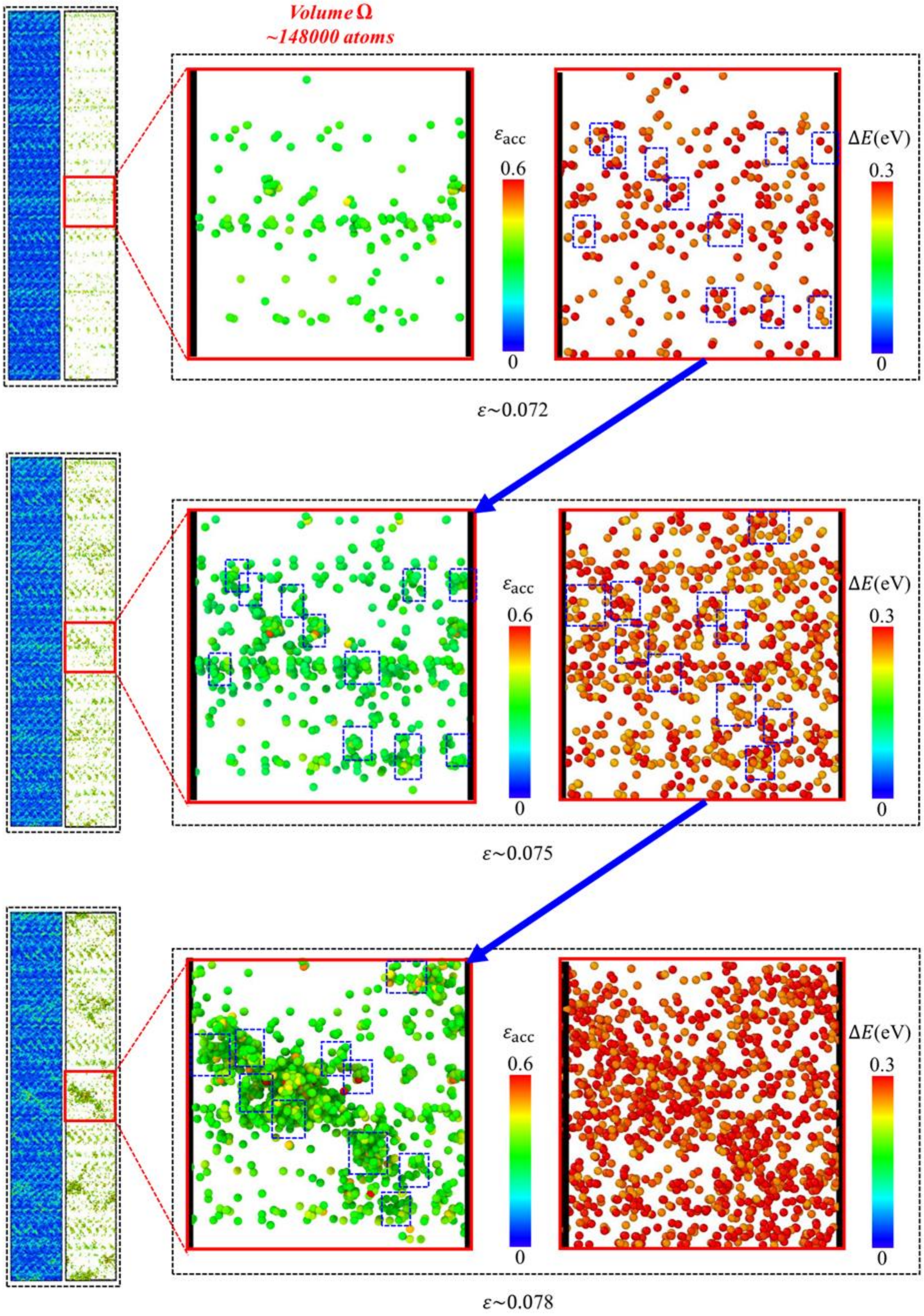
Volume Ω
~148000 atoms
$\varepsilon_{\mathrm{acc}}$
0.6
0
ΔE(eV)
0.3
0
ε~0.072
$\varepsilon_{\mathrm{acc}}$
0.6
0
ΔE(eV)
0.3
0
ε~0.075
$\varepsilon_{\mathrm{acc}}$
0.6
0
ΔE(eV)
0.3
0
ε~0.078

Figure 5. (a) MD simulated stress-strain behavior, showing noticeable yielding at overall strain of ~0.027, at which atomic-sized shear transformation zones (STZs) (marked as green) have appeared sporadically at many sites scattered throughout the sample. (b) Simulation snapshots showing formation of shear bands running across the thickness of the sample at ~ 45°, from sequential formation of nearby STZs (marked as green). The discrete STZs are identified as atomic sites around which the accumulative shear strains are over 0.2. As shown in the red-framed region, at sufficiently large straining, such discrete STZs occur preferentially very close to one another (space- and time-wise), and their coalescence forms a microscopic shear band. (c, d) Joint probability density function $p(\Delta r, \Delta t)$ of the spatial and temporal separation of the occurrence of two STZs from the MD simulation data, (c) from zero strain to the noticeable yield point at ε = 0.027, and (d) from the noticeable yield point to strain ε = 0.076 at which clear shear banding occurs. (e) Correlated emergence of STZs within the red box region Ω from snapshots 3 to 5 in (b), with overall strain ~0.072, ~0.075 and ~0.078 respectively, during shear banding. At each overall strain, the atomic positions with local accumulative strains over 0.2 are shown in the middle panel to indicate the STZs operated, and the right panel shows the positions of atoms with potential energy increments ΔE (relative to the load-free state) larger than 0.25eV. The blue boxes mark regions where ΔE is high due to proximity to operated STZs, and the blue arrows show that in the next strain increment, new STZs emerge from these high-energy regions.

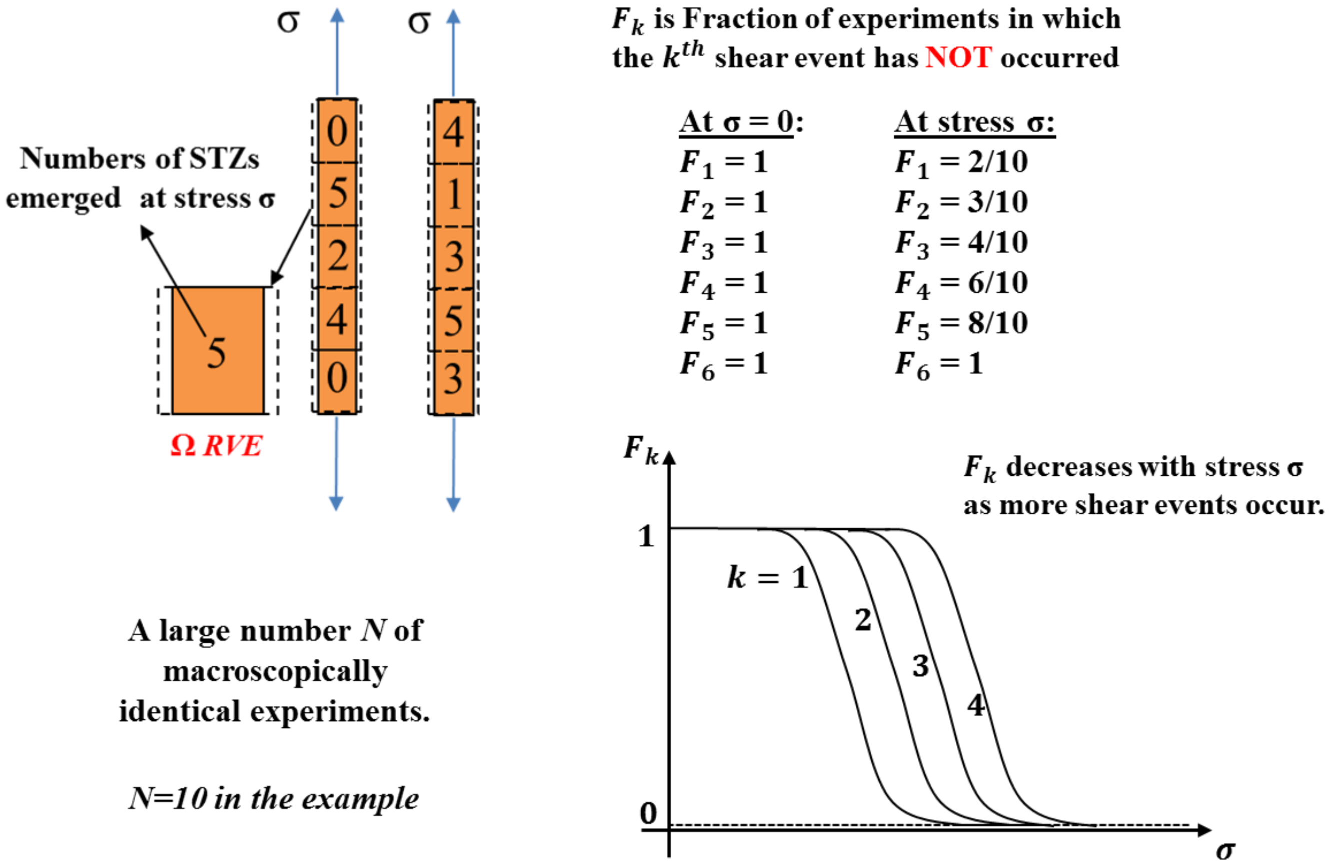

Figure 6. Schematic of the model for shear banding. Different wires are subjected to testing under the same macroscopic conditions. Along each wire, RVEs are stacked in series. In this example, 2 wires each containing 5 RVEs form an ensemble of $N = 10$ RVEs under the same macroscopic conditions. Emergence of STZs in the RVEs may not be synchronized due to their different internal structures.

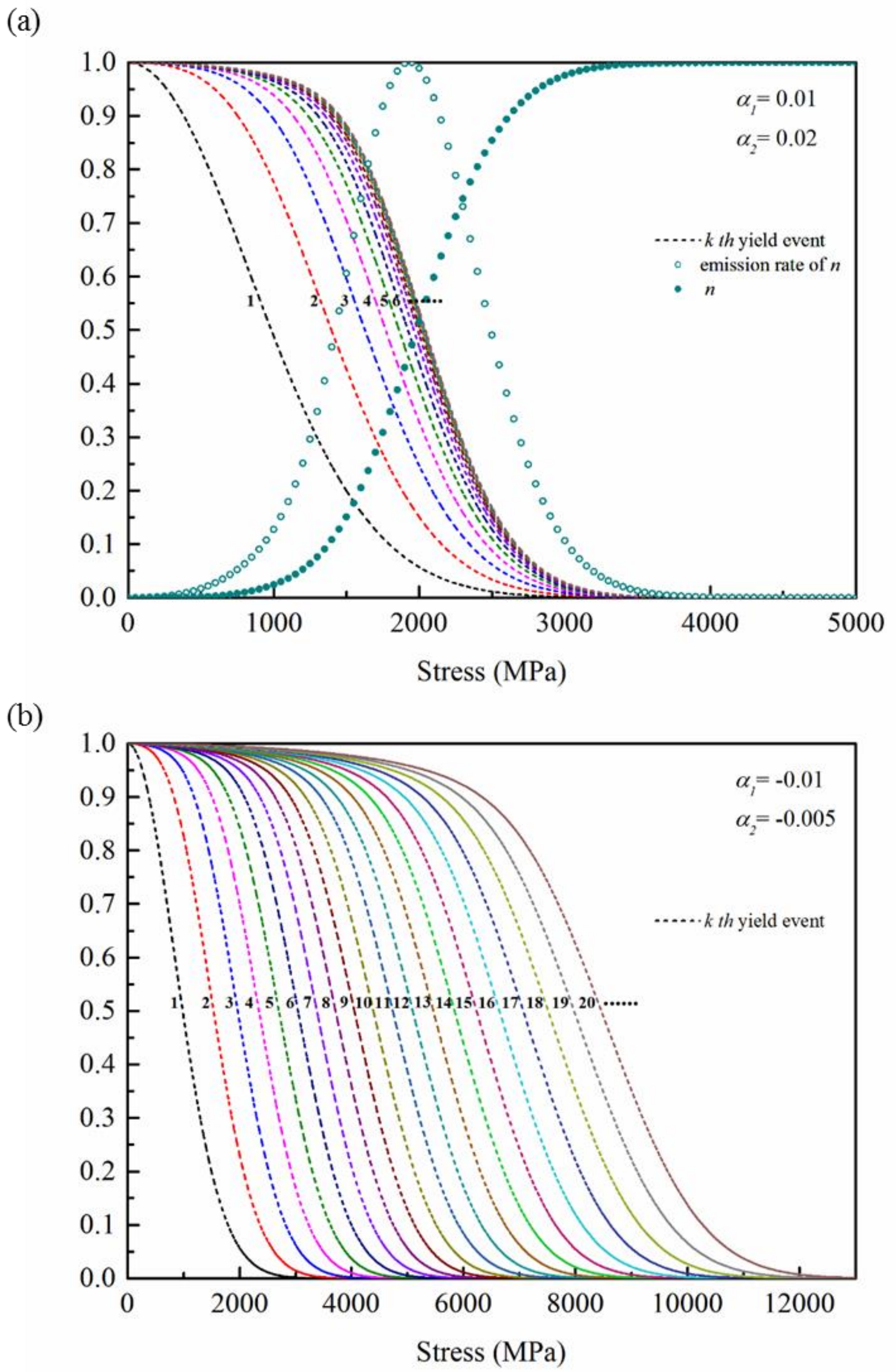

Figure 7. Examples predicted from eqns. (7) and (9) when (a) $\alpha_1, \alpha_2 > 0$ and (b) $\alpha_1, \alpha_2 < 0$ respectively. Parameters $m_1 = 2.0, v_1 = 0.01\ MPa^{-2}$ and $\Omega = 71.6 \times 10^3$ μm^3 are used in both cases. In (a), the sum of the nucleus densities $n = \sum_{j=1}^{k} n_j$ and its emergence rate $dn/d\sigma$ in the asymptotic limit $k \to \infty$ are shown, after normalization by their maximum values in the range.

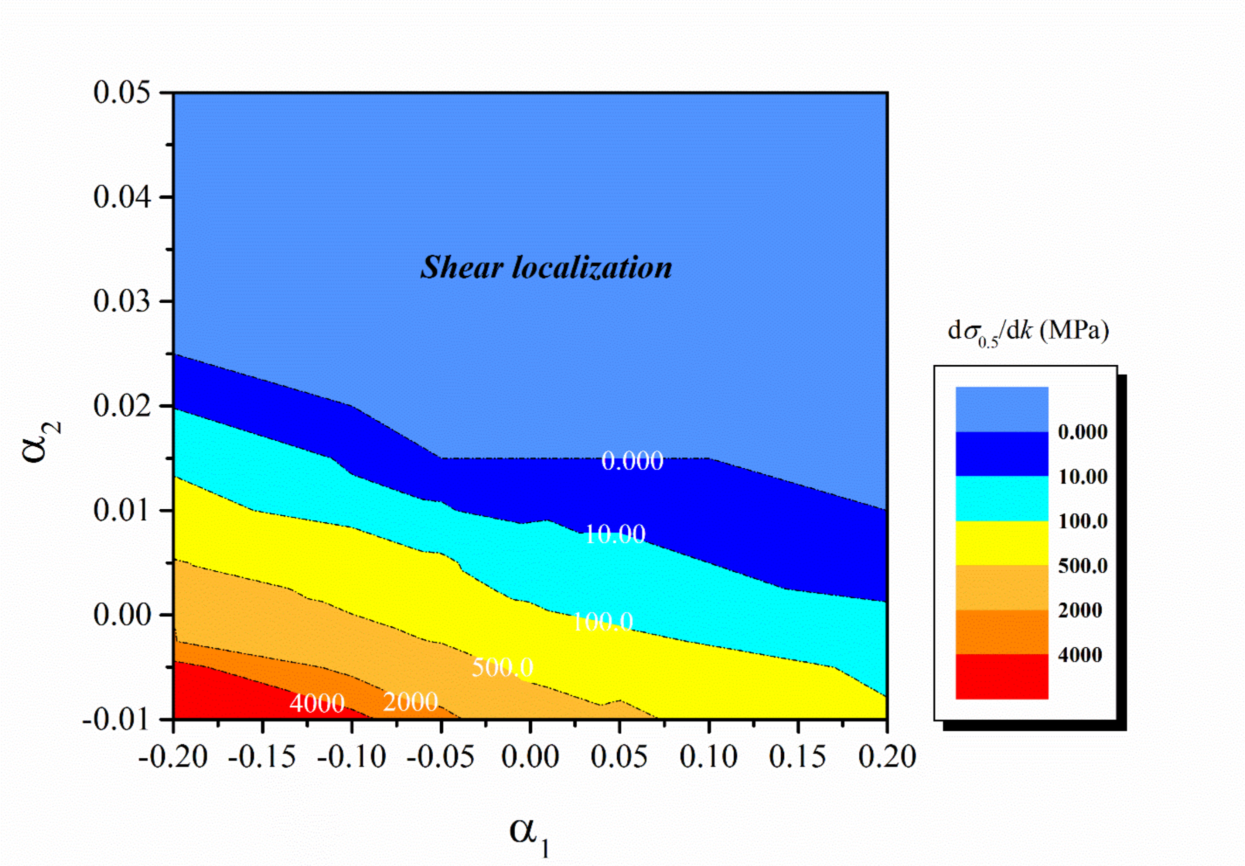

Figure 8. Factor α1-α2 mapping effect on strain localization (shear band formation) of BMG microwires. Parameters $m_1 = 2.0, v_1 = 0.01\ MPa^{-2}$ and $\Omega = 71.6 \times 10^3$ μm^3 are applied.

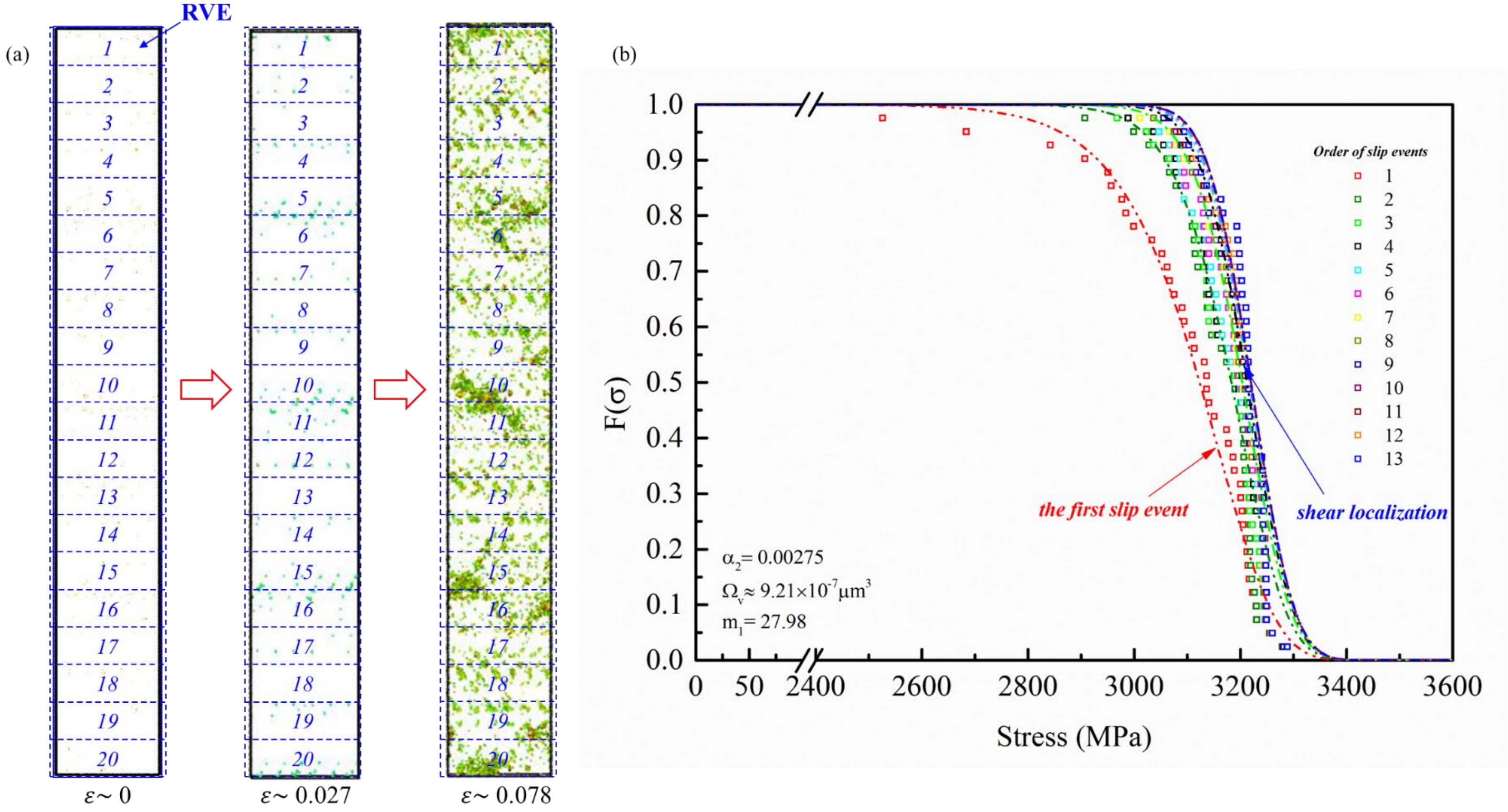

Figure 9. (a) Scheme of definition for representative volume element (RVE) belonging to a single BMG sample in MD simulation. A single glassy sample is divided into 20 adjacent but non-overlapping RVEs. (b) Computed $F(\sigma)$ curves plots through eqns. (4) with $\alpha_1 = 0, \alpha_2 = 0.00275$. The square symbol stands for the survival probability of shear events obtained through RVEs in order.

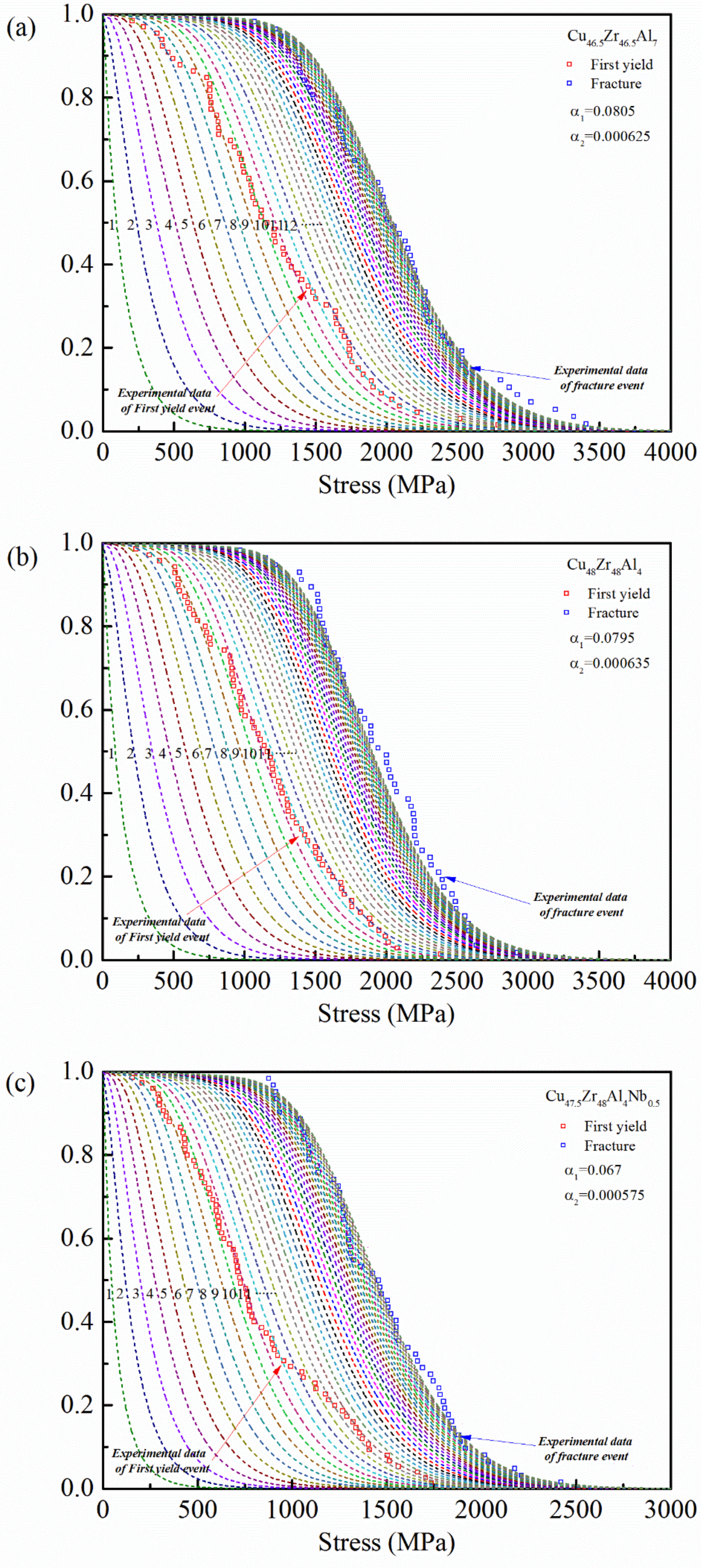
(a)
Cu46.5Zr46.5Al7
First yield
Fracture
α1=0.0805
α2=0.000625
1 2 3 4 5 6 7 8 9 10 11 12 ……
Experimental data of First yield event
Experimental data of fracture event
0.0
0.2
0.4
0.6
0.8
1.0
0
500
1000
1500
2000
2500
3000
3500
4000
Stress (MPa)
(b)
Cu48Zr48Al4
First yield
Fracture
α1=0.0795
α2=0.000635
1 2 3 4 5 6 7 8 9 10 11 ……
Experimental data of First yield event
Experimental data of fracture event
0.0
0.2
0.4
0.6
0.8
1.0
0
500
1000
1500
2000
2500
3000
3500
4000
Stress (MPa)
(c)
Cu47.5Zr48Al4Nb0.5
First yield
Fracture
α1=0.067
α2=0.000575
1 2 3 4 5 6 7 8 9 10 11 ……
Experimental data of First yield event
Experimental data of fracture event
0.0
0.2
0.4
0.6
0.8
1.0
0
500
1000
1500
2000
2500
3000
Stress (MPa)

Figure 10. (a)-(c) Computed $F(\sigma)$ plots from eqns. (4) and (6) for the tested BMG microwires with parameters (a) $\alpha_1 = 0.0805, \alpha_2 = 0.000625$, (b) $\alpha_1 = 0.0795, \alpha_2 = 0.000635$ and (c) $\alpha_1 = 0.067, \alpha_2 = 0.000575$, are used respectively.